

# 1 The architecture, assembly, and evolution of a complex flagellar motor

Xueyin Feng<sup>1,2,3,4,9</sup>, Shoichi Tachiyama<sup>5,6,9</sup>, Jing He<sup>7,9</sup>, Siqi Zhu<sup>1,2,3,9</sup>, Hang Zhao<sup>5,6</sup>, Jack M. Botting<sup>5,6</sup>, Yanran Liu<sup>1,2,3,4</sup>, Yuanyuan Chen<sup>1,2,3,4</sup>, Canfeng Hua<sup>5</sup>, María Lara-Tejero<sup>5</sup>, Matthew A. B. Baker<sup>8</sup>, Xiang Gao<sup>7,#</sup>, Jun Liu<sup>5,6,#</sup> and Beile Gao<sup>1,2,3,#</sup>

<sup>1</sup> CAS Key Laboratory of Tropical Marine Bio Resources and Ecology, Guangdong Key Laboratory of Marine Materia Medica, Innovation Academy of South China Sea Ecology and Environmental Engineering, Guangdong Provincial Observation and Research Station for Coastal Upwelling Ecosystem, South China Sea Institute of Oceanology, Chinese Academy of Sciences, Guangzhou, 511458, China

<sup>2</sup> Hainan Sanya Marine Ecosystem National Observation and Research Station and Tropical Marine Biological Research Station in Hainan, Chinese Academy of Sciences, Sanya, 572000, China

<sup>3</sup> Southern Marine Science and Engineering Guangdong Laboratory (Guangzhou), Guangzhou, 511458, China

<sup>4</sup> University of Chinese Academy of Sciences, Beijing, 100049, China

<sup>5</sup> Department of Microbial Pathogenesis, Yale School of Medicine, New Haven, CT 06536, USA

<sup>6</sup> Microbial Sciences Institute, Yale University, West Haven, CT 06516, USA

<sup>7</sup> State Key Laboratory of Microbial Technology, Shandong University, Qingdao, 266237, China

<sup>8</sup> School of Biotechnology and Biomolecular Sciences, UNSW, Kensington, Australia

<sup>9</sup>These authors contributed equally: Xuejin Feng, Shoichi Tachiyama, Jing He, Siqi Zhu.

#Correspondence: Beile Gao, gaob@scsio.ac.cn

Correspondence: Beno Gao, [gao@seis.ac.cn](mailto:gao@seis.ac.cn)  
Jun Liu, [jliu@yale.edu](mailto:jliu@yale.edu)

Xiang Gao xgao@ams

Xiang Gao, [xgao@email.sdu.edu.cn](mailto:xgao@email.sdu.edu.cn)

**Key words:** motor, stator, flagella, motility, evolution

40      **Summary (188 words)**

41

42      Bacterial flagella drive motility in many species, likely including the last bacterial common  
43      ancestor<sup>1,2</sup>. Knowledge of flagellar assembly and function has mainly come from studies  
44      of *Escherichia coli* and *Salmonella enterica*, which have simple flagellar motors<sup>3-7</sup>.  
45      However, most flagellated bacteria possess complex motors with unique, species-specific  
46      adaptations whose mechanisms and evolution remain largely unexplored<sup>8-10</sup>. Here, we  
47      deploy a multidisciplinary approach to build a near-complete model of the flagellar motor  
48      in *Campylobacter jejuni*, revealing its remarkable complexity in architecture and  
49      composition. We identify an E-ring around the MS-ring, a periplasmic cage with two  
50      distinctive conformations, and an intricate interaction network between the E-ring and cage.  
51      These scaffolds play critical roles in stabilizing and regulating 17 torque-generating stator  
52      complexes for optimal motility. In-depth evolutionary analyses uncover the ancient origin  
53      and prevalence of the E-ring in flagellated species of the domain *Bacteria* as well as a  
54      unique exaptation of type IV pili components PilMNOPQF in the ancestral motor of the  
55      phylum *Campylobacterota*. Collectively, our studies reveal novel mechanisms of assembly  
56      and function in complex flagellar motors and shed light on the evolution of flagella and  
57      modern bacterial species.

58 **Main text**

59

60 Flagellar motors are complex nanomachines that are highly diverse across bacterial species  
61 <sup>8,11,12</sup>. Among these, the classical models *E. coli* and *S. enterica* have the same, simple  
62 flagellar motor structures <sup>8,13</sup>. Between the inner membrane and outer membrane of the *E.*  
63 *coli* model, the motor is composed of an MS-ring and central rod, which is surrounded by  
64 the P-ring and L-ring at the peptidoglycan layer and outer membrane, respectively <sup>14</sup>. Motor  
65 rotation is driven by stator complexes that harness the proton motive force to generate  
66 torque <sup>15</sup>. Stator complexes are highly dynamic in *E. coli* and *S. enterica* <sup>16</sup>. Importantly,  
67 the flagellar motors in species of *Enterobacteriaceae*, including *E. coli* and *S. enterica*,  
68 were not inherited from the common ancestor of  $\gamma$ -proteobacteria but rather acquired by  
69 horizontal gene transfer from an ancestral  $\beta$ -proteobacterium <sup>17</sup>.

70

71 By contrast, the motors of many flagellated species have auxiliary structures, in  
72 addition to the P-ring and L-ring, around the rod in the periplasm <sup>18-20</sup>. Such motors with  
73 additional periplasmic scaffolds are termed complex motors and classified into three  
74 categories <sup>21</sup>: (1) outer-membrane-associated scaffold motors, as in *Vibrio* spp. that have  
75 H/T/O-rings connected to the outer membrane <sup>20,22</sup>, (2) inner-membrane-associated  
76 scaffold motors present in *Spirochaetota* species such as *Borrelia burgdorferi* (these  
77 scaffolds are known as “collars”) <sup>23-25</sup>, and (3) integrated scaffold motors spanning the  
78 periplasm and associated with both the outer membrane and inner membrane, as in *C. jejuni*  
79 and *Helicobacter pylori* <sup>9,26,27</sup>. Unlike the *E. coli* motor with its dynamic stator complexes  
80 <sup>16</sup>, complex motors possess remarkable structural intricacy that appears to stabilize stator  
81 complexes in 18 out of 24 species (Supplementary Table 1). However, the evolution and  
82 function of complex motors remain largely unknown <sup>9,28,29</sup>.

83

84 It was recently proposed that complex motors have evolved from a simple ancestral  
85 motor, whose prototype is the *E. coli* motor <sup>13,30</sup>. However, this proposal was based on  
86 motor structures in 7~8 species and on the assumption that the ancestral motor should be  
87 the simplest <sup>13,30</sup>. Evidence from bacterial phylogeny does not align with this notion <sup>31</sup> and  
88 is confounded by differences in specific proteins and structures across species. To better  
89 understand the evolutionary path and mechanism of complex motors, the first challenge is  
90 to identify components that constitute the additional structures. The motility of the human  
91 pathogen *C. jejuni* is driven by a complex flagellar motor in each cell pole <sup>32</sup>. The complex  
92 flagellar motor of *C. jejuni* has a well-studied “parts list”, thanks to multiple high-  
93 throughput transposon library screenings and extensive characterization of novel flagellar  
94 genes <sup>9,26,33-36</sup>. Notably, our previous Tn-seq screenings using cell invasion and mouse  
95 infection identified several novel genes impacting motility, including those that, when  
96 deleted, result in a significant decrease in fitness during host interaction but no change in  
97 motility on artificial soft agar or liquid medium <sup>33,37</sup>.

98

99        The *C. jejuni* motor contains three disks: a basal disk composed of FlgP just below the  
100 outer membrane<sup>9,38</sup>, a medial disk composed of PflC and PflD<sup>26</sup>, and a proximal disk  
101 containing PflA and PflB<sup>9,26</sup>. These findings provided a foundation to dissect complex  
102 motors with homologs and suggested that complex motors possess mechanisms different  
103 from those in the classical model<sup>30,38,39</sup>.

104

### 105 **Mapping the components in motor periplasmic scaffolds by imaging specific mutants**

106        We structurally characterized new periplasmic scaffold proteins in the *C. jejuni* motor by  
107 using cryo-electron tomography (cryo-ET) and molecular genetics. Among multiple  
108 flagellar genes identified from Tn-seq screenings<sup>33,37</sup>, mutants of *flgY*(*CJJ81176\_1488* in  
109 *C. jejuni* 81-176 genome)<sup>33</sup> and three genes in a cluster (*CJJ81176\_0481, 0480, 0479*)<sup>37</sup>  
110 showed loss of specific densities in the periplasmic region of the flagellar motor structures,  
111 with all other scaffolds remaining largely intact, as in wild type (Fig. 1a-d).

112

113        Compared to the wild-type motor, the  $\Delta flgY$  motor lacks a periplasmic spoke-ring  
114 around the MS-ring (Fig. 1a-c), a location like that of the “E-ring” first discovered by  
115 electron microscopy in *Caulobacter crescentus*<sup>40,41</sup>. Extensive classification and  
116 refinement of the periplasmic region of the wild-type *C. jejuni* motor structure revealed  
117 that the E-ring is not a continuous ring or disk. Instead, it is composed of a small, thin ring  
118 around the MS-ring and 17 separate spokes radiating from the small ring (Fig. 1b). These  
119 spokes connect in a 1:1 ratio with 17 longer, distal spokes that extend to 17 stator  
120 complexes and attach to a continuous rim-like structure (Fig. 1b). The distal spokes and  
121 rim are composed of PflA (spokes) and PflB (rim)<sup>26</sup>. In addition, an N-terminal 17-aa  
122 signal peptide was predicted for FlgY (Extended Data Fig. 1a). Thus, FlgY is likely a  
123 periplasmic component of the E-ring.

124

125        The triple knockout mutant  $\Delta CJJ81176\_0481-0479$  lacks the peripheral structure most  
126 distal from the central rod in wild-type *C. jejuni* (Fig. 1a,b,d). This peripheral structure is  
127 made of 34 units embedded in the inner membrane and below the medial disk (Fig. 1a,b).  
128 The position and shape of this structure are very similar to those of the lower cage in *H.*  
129 *pylori*, which consists of PilM/PilN/PilO homologs of type IV pili (T4P)<sup>42</sup>. Sequence  
130 analyses and AlphaFold3 structure prediction of *CJJ81176\_0481, 0480, and 0479* revealed  
131 that these three proteins in *C. jejuni* are homologs of *H. pylori* PilM/PilN/PilO (Extended  
132 Data Fig. 1b,c). Coimmunoprecipitation (co-IP) followed by liquid chromatography-mass  
133 spectrometry (LC-MS/MS) analysis also revealed that each protein can pull down the other  
134 one or two proteins in *C. jejuni*, suggesting that they form a complex (Supplementary Table  
135 2). In addition, *C. jejuni* 81-176 does not encode other components of T4P, and these three  
136 genes show co-occurrence with the ancient flagellar gene set and F3 chemosensory class  
137 in genomes of *Campylobacterota* species (discussed in detail in later section). Hence, we  
138 named the proteins *CJJ81176\_0481, 0480, and 0479* flagellar cage proteins  
139 *FcpM/FcpN/FcpO*, based on their shared homology with PilM/PilN/PilO but different roles

140 as flagellar components.

141

142 To explore the structural dependency of these new scaffolds with surrounding  
143 structures, such as the proximal and medial disks made of PflA/PflB/PflC/PflD, we  
144 compared the motor structures of four mutants:  $\Delta pflA$ ,  $\Delta pflB$ ,  $\Delta pflC$ , and  $\Delta pflD$  (Fig. 1e-h). In  $\Delta pflA$ , only the E-ring is present with more plasticity in shape in the inner-membrane  
145 proximal region, while the PflA spokes, PflB rim, and cage units are absent (Fig. 1e). For  
146  $\Delta pflB$ , both the E-ring and spokes remain, but with less resolved densities, while the rim  
147 and cage units are missing (Fig. 1f). The  $\Delta pflD$  mutant mimics  $\Delta fcpMNO$ , missing the  
148 entire peripheral cage. (Fig. 1d,h). Though not as stable as those in the wild-type motor,  
149 the E-ring, spokes, and rim remain in the  $\Delta pflC$  mutant (Fig. 1g), in contrast to the complete  
150 scaffold loss recently reported<sup>26</sup>. Together, these findings establish that assembly of the E-  
151 ring is not dependent on PflA/PflB/PflC/PflD or FcpM/FcpN/FcpO and that the full set of  
152 34 peripheral cage units requires all scaffolds inside (PflA/PflB/PflC/PflD) except the E-  
153 ring.  
154

155

156 To determine the roles of the scaffolds in motor function and bacterial motility, we  
157 compared the stator densities of seven mutants and wild-type *C. jejuni* (Fig. 1b-i). The  $\Delta flgY$   
158 mutant showed the same stator density as wild type, with approximately 80% of the motors  
159 having a full stator ring and remaining 20% having less-resolved stator densities (Fig. 1b,c  
160 and Extended Data Fig. 2a). By contrast, neither the  $\Delta pflA$  nor  $\Delta pflB$  mutant has stator  
161 densities in the motor structure, similar to  $\Delta motA$  (Fig. 1e,f,i). The three mutants  $\Delta pflC$ ,  
162  $\Delta pflD$ , and  $\Delta fcpMNO$  have reduced stator densities (Fig. 1d,g,h). Specifically,  
163 approximately 10% of the  $\Delta pflD$  and  $\Delta fcpMNO$  mutants have stator complexes loaded in  
164 the motor, and the  $\Delta pflC$  mutant has least stator complexes in the motor (Extended Data  
165 Fig .2a and Fig. 1d,g,h). Importantly, the differences in stator density/occupancy among  
166 these mutants are consistent with their motility phenotypes on soft agar, including the  
167 greatly reduced but not abolished motility of the  $\Delta pflC$  mutant (Extended Data Fig. 2b).  
168 Collectively, our data provide direct evidence that the inner-membrane scaffolds are critical  
169 for stator assembly and motility in *C. jejuni* (Fig. 1 and Extended Data Fig. 2).

170

### 171 **FlgY dimers form the E-ring around the MS-ring via ARM-like domains**

172 Next, we dissected the structure, function, and interaction of the inner-membrane proximal  
173 scaffolds at the protein or domain/motif level. Starting from the innermost E-ring,  
174 candidate component FlgY was structurally analyzed. AlphaFold3 prediction showed that  
175 FlgY is entirely  $\alpha$ -helical, with the N-terminal 15-116 aa forming a long  $\alpha$ -helix and the  
176 remaining 56 residues comprising a four-membered, right-handed superhelix (Fig. 2a). The  
177 superhelical domain contains a hydrophobic core, showing structural similarity to the N-  
178 terminal cytosolic domain of the Mg<sup>2+</sup> transporter MgtE as well as to the armadillo repeat  
179 motif (ARM)-like motifs in flagellar rotor protein FliG (Extended Data Fig. 3a)<sup>43-45</sup>. In  
180 particular, this C-terminal domain, here named FlgY<sub>ARM</sub>, differs from the canonical ARM

181 repeat with regard to helical packing<sup>44,45</sup> and matches well with the ARM-like motif of  
182 MgtE and FliG (Extended Data Fig. 3a,b).

183

184 Purified FlgY without the predicted signal peptide (FlgY<sub>15-172</sub>) forms a dimer in  
185 solution (Extended Data Fig. 3c). In addition, variants with different truncations in the N-  
186 terminal long  $\alpha$ -helix region still form a dimer, suggesting that the FlgY dimer is stable  
187 even without the long  $\alpha$ -helix region (Extended Data Fig. 3c). ARM repeats stack on each  
188 other intramolecularly or intermolecularly, as shown for ARM-like motifs in FliG that drive  
189 C-ring formation<sup>46,47</sup>. To test whether FlgY<sub>ARM</sub> shares the same feature, crosslinking  
190 experiments were carried out on FlgY<sub>15-172</sub> and FlgY<sub>ARM</sub>. Both can form higher oligomers  
191 (Extended Data Fig. 3d), suggesting that dimeric FlgY<sub>ARM</sub> may stack with an adjacent  
192 FlgY<sub>ARM</sub> as well. We then docked the predicted structure of the FlgY dimer into a refined  
193 cryo-ET map at 12 Å resolution (Fig. 2b-d and Extended Data Fig. 3e). 34 ARM-like  
194 domains from 17 FlgY dimers form a ring around the  $\beta$ -collar of the MS-ring, and each  
195 dimeric coiled coil domain points outward, interacting with the distal spoke formed by PflA  
196 (Fig. 2d-g). This interaction between FlgY and PflA is consistent with the additional  
197 densities at the inner end of the PflA spokes in the  $\Delta flgY$  mutant (Fig. 2f,g and 1c).  
198 Additionally, the interaction of PflA with FlgY<sub>15-172</sub>, but not with FlgY<sub>ARM</sub> without the N-  
199 terminal long  $\alpha$ -helix, was detected by microscale thermophoresis (Extended Data Fig. 3f).  
200 These results suggest that FlgY dimers constitute the E-ring and connect with PflA spokes  
201 via the long  $\alpha$ -helix region.

202

### 203 **PflA spokes tightly bind the PflB rim**

204 To determine how the spokes interact with the rim, we improved *in-situ* structure of the  
205 spoke-rim complex at 12 Å resolution by 17-fold symmetry expansion and focused  
206 refinement (Fig. 2e) in addition to solving a single particle cryo-EM structure of the PflAB  
207 complex at 3.23 Å resolution (Fig. 2h,i, Extended Data Fig. 4). A combination of both *in-*  
208 *situ* and *in-vitro* structures with AlphaFold3 prediction of PflA enabled us to build the  
209 pseudoatomic model of the spoke-rim complex (Fig. 2f,g). In this model, PflA and PflB  
210 are in a 1:1 ratio, with the majority of PflB (178-820 aa) resolved at near-atomic resolution  
211 (Fig. 2h). PflB is mainly composed of tetratricopeptide (TPR) repeats and can be divided  
212 into two parts by a  $\beta$ 1-sheet (aa 386-390) (Fig. 2h). The N-terminal TPR repeats before the  
213  $\beta$ 1-sheet are relatively extended, while those after the  $\beta$ 1-sheet are tightly packed (Fig. 2h).  
214 Notably, the last 5 C-terminal residues form a  $\beta$ 2-sheet (aa 813-817) that makes an  
215 antiparallel  $\beta$ -pair with the  $\beta$ 1-sheet (Fig. 2h). This antiparallel  $\beta$ -pair resembles a “hook  
216 and loop”, as the two  $\beta$ -sheets are separated by 423 residues in sequence yet  
217 engaged together in the 3D structure (Fig. 2h). We hypothesize that this  $\beta$ -pair stabilizes  
218 the TPR repeats after the  $\beta$ 1-sheet, making it less extended than the N-terminus in overall  
219 shape (Fig. 2h).

220

221 PflA consists of the N-terminal  $\beta$ -sandwich domain, flexible loop, and C-terminal 17

222 repetitive TPR repeats. The N-terminal  $\beta$ -sandwich domain and flexible loop region (16-  
223 163 aa) are resolved in our cryo-EM structure (Fig. 2h,i). The  $\beta$ -sandwich domain of PflA  
224 is made of four pairs of antiparallel  $\beta$ -sheets and here named PflA<sub>AMIN</sub> for its resemblance  
225 to the AMIN1 and AMIN2 domains of PilQ in T4P (Extended Data Fig. 5a). Interestingly,  
226 the long loop of PflA (126-163 aa) wraps around the N-terminal extended TPR repeats of  
227 PflB, mainly via hydrophobic contacts (Fig. 2i and Extended Data Fig. 5b). The critical  
228 role of this PflA loop in PflB interaction was further confirmed by bacterial two hybrid  
229 (BTH) analyses (Fig. 2j). Overall, the PflAB complex is akin to a “wire-wrapped pendant”,  
230 with PflA (wire) looping around PflB (stone), forming a tight interaction (Fig. 2i) and  
231 assembling the PflAB spoke-rim (Fig. 2g).

232

233 To dissect the role of each domain and/or motif in the PflAB complex, various  
234 truncations of PflA or PflB were made and complemented into the  $\Delta pflA$  or  $\Delta pflB$  mutant,  
235 respectively, for soft agar motility assays (Extended Data Fig. 5c). Results show that  
236 PflA<sub>AMIN</sub> and the first 15 TPR repeats are important for PflA function because their deletion  
237 results in a non-motile phenotype (Extended Data Fig. 5c). Our PflAB complex structure  
238 suggests that these two regions are not involved in PflB interaction, a finding further  
239 confirmed by BTH analyses (Fig. 2h-j). Notably, PflA was detected in the co-IP product of  
240 3xFLAG-tagged FcpO (Supplementary Table 2), implying that PflA spokes interact with  
241 the cage units in addition to the rim. To test this notion, we performed BTH analyses for  
242 PflA and the PflA<sub>AMIN</sub> domain with multiple scaffolding proteins in the peripheral region.  
243 Results show that the PflA<sub>AMIN</sub> domain, but not the whole periplasmic region of PflA, can  
244 interact with FcpO and FliL (Extended Data Fig. 5d).

245

246 Finally, removal of the N-terminal cytoplasmic region of PflB reduced motility to 50%  
247 of wild-type levels on soft agar, suggesting that this region plays a role in PflB function,  
248 perhaps interacting with other protein(s) in the cytosol (Extended Data Fig. 5c). Deletion  
249 of the  $\beta$ 2-sheet from PflB results in complete loss of motility (Extended Data Fig. 5c),  
250 supporting a structural role for the  $\beta$ -pair in PflB (Fig. 2h).

251

## 252 **Two PflD conformations form different tetrameric cage units with FcpMNO**

253 Our recent study revealed that the number of peripheral cage units is reduced to 17 in both  
254 the  $\Delta motA$  and  $\Delta flgX$  mutants, half the number in the wild-type motor (Fig. 1i)<sup>48</sup>. We  
255 proposed that half of the cage units assemble after stator association, but it remained  
256 unknown how the FcpMNO proteins might achieve this two-step assembly. Here, we  
257 compared the refined structures of the peripheral cage region of wild type and three mutants:  
258  $\Delta fcpMNO$ ,  $\Delta motA$ , and  $\Delta pflD$  (Fig. 3a). In wild type and the  $\Delta fcpMNO$  and  $\Delta motA$  mutants,  
259 17 density spots are present below the medial disk (just below the PflC<sub>2-6</sub> radial spokes<sup>26</sup>)  
260 but missing from the  $\Delta pflD$  mutant (Fig. 3a and Extended Data Fig. 6a). Therefore, these  
261 17 spots likely represent PflD, consistent with the proposed position for PflD in a recent  
262 study that also indicated a density of unknown composition next to PflD<sup>26</sup>. We examined

263 this unknown density between two cage units and found that it is absent from all three  
264 mutants, including  $\Delta motA$ , suggesting that it is related to the missing cage units and stator  
265 complexes in the  $\Delta motA$  mutant (Fig. 3a and Extended Data Fig. 6a).

266

267 PflD contains an N-terminal transmembrane motif, and its structure predicted by  
268 AlphaFold3 has a C-terminal globular domain similar to the N1 domain of PilQ from T4P  
269<sup>49</sup> (Extended Data Fig. 6b). Between the transmembrane motif and C-terminal PflD<sub>PilQ-N1</sub>  
270 domain is a 60 aa flexible loop very similar to the loop region of PilP (named PflD<sub>PilP-loop</sub>)  
271<sup>49</sup> (Extended Data Fig. 6b). A recent study on the T4P structure of *Pseudomonas aeruginosa*  
272 suggested that PilP interacts with PilNO via its short  $\alpha$ -helix, together forming a tri-helix  
273 bundle-like structure<sup>49</sup>. Alphafold3 prediction for PflD and FcpNO also showed a tri-helix  
274 bundle, but one formed by the N-terminal transmembrane segments of all three proteins  
275 (Extended Data Fig. 6c). This predicted complex appears more stable than PilNOP because  
276 PilP lacks a transmembrane motif and has a limited interaction interface with PilNO<sup>49</sup>  
277 (Extended Data Fig. 6c).

278

279 As a flexible loop, PflD<sub>PilP-loop</sub> can be stretched or contracted, leading us to speculate  
280 that PflD in contracted form is the unknown component between the two cage units in wild  
281 type (Fig. 3b). To test this notion, the predicted PflD-FcpNO trimer structures in both  
282 stretched and contracted conformations were docked into our cryo-ET density map of the  
283 wild-type motor in alternating order (Fig. 3b,c). Both conformations fit very well with the  
284 periphery structure below the medial disk, specifically with the PflD<sub>PilQ-N1</sub> domain  
285 positioned in the 17 density spots as recently proposed<sup>26</sup> and also the other 17 densities  
286 between two cage units (Fig. 3c). We also detected interaction between PflD and FcpN and  
287 PflD and FcpO with all their transmembrane motifs included using BTH analyses, but no  
288 interaction between these protein pairs with only their periplasmic regions (Extended Data  
289 Fig. 6d). Therefore, we propose that the peripheral cage units are heteromeric tetramers  
290 made of FcpMNO and PflD, with PflD in alternating extended and contracted  
291 conformations. Moreover, the cryo-ET structure suggests that PflD with extended PflD<sub>PilP-</sub>  
292 <sub>loop</sub> reaches to the PflC<sub>2-6</sub> spokes above via its PflD<sub>PilQ-N1</sub> domain, possibly linking 17 of  
293 the cage units to the medial disk (Fig. 3b,c). This linkage may be one reason why the half  
294 of the cage units with extended PflD<sub>PilP-loop</sub> remain in the motor upon deletion of *motA*,  
295 while the other half fail to assemble in the absence of stator complexes (Fig. 3a).

296

### 297 **The model and dynamics of the complex flagellar motor in *C. jejuni***

298 The above findings by the integrated approach allowed us to build a near-complete  
299 pseudoatomic structure of the *C. jejuni* motor (Fig. 4a). In this model, FlgY dimers,  
300 together with PflA monomers, form 17 spokes radiating from the MS-ring to connect 17  
301 stator complexes in the motor (Fig. 4b,c). Around the stator complexes, one L-shaped PflA  
302 binds one PflB via its flexible loop, locking 17 PflB monomers into a continuous rim that  
303 holds 17 MotB dimers (Fig. 4b,c). Peripheral to the stator ring and rim, 34 cage units made

304 of FcpMNO and PflD further enclose the stator complexes (Fig. 4b,c). Towards the top  
305 section, 17 cage units with extended PflD<sub>PilP-loop</sub> connect with 17 PflC<sub>2-6</sub> spokes in the  
306 medial disk (Fig. 4a). Towards the bottom section, all proteins PflB, FliL, FcpN, FcpO, and  
307 PflD have a transmembrane motif, and thus the scaffolds they form include one rim, 17  
308 FliL rings, and 34 cage units all anchored in the inner membrane (Fig. 4a). In addition,  
309 these proteins together with PflA form a complex interaction network, as suggested by our  
310 BTH analyses (Extended Data Fig. 5d and 6d). Overall, this scaffolding platform resembles  
311 a lattice (such as the "Hanging Gardens of Babylon") with load-bearing beams (FlgY/PflA)  
312 and multiple pillars (PflB/FliL/FcpNO/PflD) embedded in the inner membrane, stably  
313 accommodating 17 stator complexes within the *C. jejuni* motor (Fig. 4a,b).

314

315 Notably, the peptidoglycan layer is not visible inside the motor. It seems clear that the  
316 periplasmic scaffolding platform encloses the stator complexes while excludes the  
317 peptidoglycan layer (Fig. 1b, 4a). Intriguingly, PflA contains a peptidoglycan-binding  
318 module, PflA<sub>AMIN</sub> domain<sup>49-51</sup>, which could remain in contact with the peptidoglycan layer  
319 through the gaps between the cage subunits (Fig. 4). By contrast, MotB is completely  
320 separated from the peptidoglycan layer due to the presence of the periplasmic scaffolds  
321 including FliL ring, PflA spokes, PflB rim, and FcpMNO/PflD cage (Fig. 4a). Therefore,  
322 the *C. jejuni* motor must utilize a different mechanism to control stator activation without  
323 directly interacting the peptidoglycan layer.

324

325 Importantly, focused classification enabled us to uncover conformational changes *en*  
326 *bloc* in wild-type *C. jejuni* motors (Supplementary Video 1, 2). Specifically, focused  
327 classification on the periplasmic scaffolds revealed their variable height relative to the MS-  
328 ring and rod, reflecting plasticity and adaptation of the motor to accommodate slight  
329 variation in the bacterial envelope (Extended Data Fig. 7a-d and Supplementary Video 1).  
330 Focused classification on the C-ring not only revealed its 40 subunits but captured their  
331 distinct orientations (Extended Data Fig. 7e and Supplementary Video 2), different from  
332 the 38-fold symmetry recently reported for *C. jejuni* C-ring<sup>26</sup>. Given that the wild-type  
333 motors rotate constantly, a sequentially arranged image stack enabled us to visualize the  
334 motor rotation and dynamic fluctuations for the first time (Supplementary Video 2).

335

### 336 **Inner-membrane proximal scaffolds and stator complexes assemble before the rod in 337 *C. jejuni***

338 In the classical model, assembly follows an inside-out sequence across the cell envelope<sup>52</sup>.  
339 For complex motors, investigations of how and in what order the periplasmic scaffolds  
340 assemble are limited to a pilot study in *B. burgdorferi*<sup>53</sup>. In *C. jejuni*, RpoN ( $\sigma^{54}$ ) and FliA  
341 ( $\sigma^{28}$ ) are specific regulators for flagellar gene expression<sup>32,54</sup>. To explore the gene  
342 regulation of the inner-membrane proximal scaffolds, we performed RNA-seq on wild-type  
343 *C. jejuni* as well as  $\Delta rpoN$  and  $\Delta fliA$  mutants. Compared to the wild-type  
344 transcriptome, the expression levels of *flgY*, *pflA*, *pflB*, and *fcpM* remained the same in both

345 mutants, while *fcpN*, *fcpO* and *pflD* showed a 2-fold decrease in the  $\Delta rpoN$  mutant (Fig. 5a  
346 and Supplementary Table 3). The relative transcript abundance of *fcpN* and *fcpO* was very  
347 low in all samples examined (Supplementary Table 3), so we performed qPCR analyses for  
348 all seven genes to verify the RNA-seq data (Extended Data Fig. 8a). Our qPCR results  
349 show that none of these genes encoding for inner-membrane proximal scaffolds are  
350 regulated by RpoN or FliA (Extended Data Fig. 8a). In addition, no RpoN- or FliA-binding  
351 motifs were found in the promoter regions of *flgY*, *pflA*, *pflB*, *pflD*, or *fcpMNO* (Extended  
352 Data Fig. 8b). Therefore, genes encoding the E-ring, spokes, rim, and cage are outside the  
353 known flagellar transcriptional cascade in *C. jejuni* (Fig. 5b).

354

355 As RpoN is an early checkpoint during flagellar assembly, the motor structure of the  
356  $\Delta rpoN$  mutant was examined by cryo-ET to gain detail for complex motor intermediates.  
357 Consistent with the RNA-seq data, the flagellar type III secretion system, C-ring, MS-ring,  
358 and inner-membrane proximal scaffolds are clearly visible in the  $\Delta rpoN$  mutant, which  
359 lacks a rod and other periplasmic and extracellular structures (Fig. 5c). Importantly, the  
360 stator complexes seem to partially occupy the  $\Delta rpoN$  motor, with less-resolved densities  
361 and incomplete FliL rings also present (Fig. 5c). The early assembly of these structures is  
362 also supported by a recent cryo-ET study showing flagellar intermediate structures  
363 containing the “MS-complex”, cage, and stator complexes without the rod in wild-type *C.*  
364 *jejuni* and *H. pylori*<sup>55</sup>.

365

366 A novel density, a continuous ring without clear symmetry, also exists above the MS-  
367 ring and E-ring in the  $\Delta rpoN$  mutant (Fig. 5c). This is likely a transient periplasmic ring  
368 that has not been reported previously in any species or in the fully assembled motor.  
369 Though its composition remains to be determined, it likely assists assembly of the rest of  
370 the basal body.

371

### 372 **Inner-membrane proximal scaffolds likely existed in the ancestral flagellar motor of** 373 ***Campylobacterota***

374 To address the origin of the intricate inner membrane-anchored scaffold network in *C.*  
375 *jejuni*, we first analyzed the distribution of scaffolding proteins in representative species of  
376 the phylum *Campylobacterota*. This phylum is ecologically diverse, spanning from deep-  
377 sea hydrothermal vents to terrestrial environments and various hosts<sup>31,56</sup>. Homologs of  
378 FlgY and PflA are present in all species of this phylum except six species without a flagellar  
379 gene set; PflB homologs are missing from species that either lack a flagellar gene set or  
380 belong to the genus *Nitratiruptor* but are present in all the remaining species; homologs of  
381 PflD and the three unfused proteins FcpM/FcpN/FcpO exist in most species of this phylum  
382 (59 out of 82 species) (Supplementary Table 4)<sup>31</sup>. Importantly, the genes that flank *flgY*,  
383 *pflA*, *pflB*, *pflD*, and *fcpMNO* are also conserved across the genomes (Fig. 6a, Extended  
384 Data Fig. 9 and 10).

385

386 Next, the presence of homologs was mapped to the phylogenetic tree of  
387 *Campylobacterota*<sup>31</sup>. In the context of species evolution, information for the chemosensory  
388 system and the whole flagellar gene set was also added to provide a genomic background  
389 for our proteins of interest<sup>31</sup> (Fig. 6b, Extended Data Fig. 9 and 10). Clearly, species that  
390 have all seven proteins (FlgY, PflA, PflB, PflD, and unfused FcpM/FcpN/FcpO) also have  
391 the F3 class of the chemosensory system, which co-evolved with the ancestral flagellar  
392 gene set in this phylum, based on our previous studies<sup>31</sup> (Fig. 6b, Extended Data Fig. 9  
393 and 10). To examine the association of FcpM/FcpN/FcpO homologs with flagella or T4P,  
394 genes that encode T4P components were searched for in all representative genomes of  
395 *Campylobacterota*. The T4P gene set can be identified in half of the species of this phylum,  
396 but their species distribution pattern is distinct from FcpM/FcpN/FcpO homologs  
397 (Extended Data Fig. 10 and Supplementary Table 4). In particular, all T4P gene clusters  
398 have the same gene order *pilMNOPQ*, and most have *pilM* and *pilN* fused into one gene  
399 (Extended Data Fig. 10). By contrast, *fcpMNO* is an independent operon with conserved  
400 upstream gene *miaB*, and this operon is present in all species with a flagellar gene set,  
401 regardless of the presence of the T4P gene set (Extended Data Fig. 10). Hence, based on  
402 their strict co-occurrence with the flagellar gene set, rather than T4P, in *Campylobacterota*  
403 genomes, we conclude that FcpM, FcpN, and FcpO are flagellar proteins in this phylum.  
404

405 Altogether, inner-membrane proximal scaffold components are conserved in  
406 *Campylobacterota*. Structures composed of these components are likely present in other  
407 species of this phylum that inherited the ancestral flagellar gene set and F3 chemosensory  
408 class<sup>31</sup>. In addition, these scaffolds likely existed in the common ancestor of  
409 *Campylobacterota*.

410

#### 411 **The E-ring and spokes are ancient and widespread in the *Bacteria* domain**

412 We then extended our phylogenetic analyses of scaffolding proteins to 2,638 representative  
413 species of the *Bacteria* domain, covering a great diversity of phyla/superphyla. Among the  
414 1,365 species with a flagellar gene set, 66% have a FlgY homolog, while most species  
415 without FlgY come from two lineages: β- and γ-proteobacteria (Fig. 6c and Supplementary  
416 Table 5). Unlike FlgY with its conserved ARM-like domain and relatively conserved gene  
417 order in various genomes (Extended Data Fig. 11), neither PflA nor PflB is conserved at  
418 the sequence level. Lack of sequence conservation is a feature of TPR repeats, hindering  
419 their identification by homology search<sup>57</sup>. Thus, we considered proteins with many TPR  
420 repeats that lie within or in proximity to flagellar gene clusters as potential PflA and PflB  
421 homologs. Among the species with a set of flagellar genes, approximately 52% contain  
422 TPR repeat proteins possibly related to flagella, which may be an underestimate due to the  
423 criterion of proximity to flagellar genes (Fig. 6c and Supplementary Table 5). In addition,  
424 most of these genomes have only one copy of a TPR repeat protein in proximity to flagellar  
425 genes. Structurally, this single-copy TPR repeat protein is more similar to PflA than PflB  
426 because it lacks the defining feature of PflB here, which is the presence of both a

427 transmembrane motif and antiparallel  $\beta$ -sheet pair in the middle of the 3D structure  
428 (Extended Data Fig. 12).

429

430 The wide distribution of FlgY and potential PflA homologs in flagellated bacterial  
431 species across phyla suggests that the E-ring and spokes are a common structure in flagellar  
432 motors outside  $\beta$ - and  $\gamma$ -proteobacteria. Notably, several flagellar proteins in species of  
433 distantly related  $\alpha$ -proteobacteria and *Spirochaetota* are FlgY or PflAB homologs based on  
434 structural similarity (Extended Data Fig. 11 and 12). This homologous relationship was not  
435 previously known due to low sequence homology, but the periplasmic location, protein-  
436 protein interaction, and functional relationship with stator complexes of these proteins  
437 previously reported<sup>23,24,58,59</sup> agree with our findings for FlgY and PflAB. In addition,  
438 homologs for FlgY and PflA exist in the genome of *C. crescentus* (CC\_2059 and CC\_2058),  
439 with the corresponding genes adjacent to each other (Extended Data Fig. 11 and 12),  
440 confirming that the “E-ring” in isolated basal bodies of this species consists of FlgY and  
441 PflA<sup>40,41</sup>.

442

443 In contrast to the wide presence of FlgY and potential PflA homologs across different  
444 bacterial phyla, homologs of FcpM, FcpN, FcpO, and PflD were only found in  
445 *Campylobacterota* (Fig. 6c). Thus, the cage is a unique structure in flagellated species of  
446 *Campylobacterota*, likely evolved in the common ancestor of this phylum. Remarkably,  
447 the ancestral motor of *Campylobacterota* likely had multiple components from T4P,  
448 including the PflA<sub>AMIN</sub> and PflD<sub>PilQ-N1</sub> domains from PilQ, PflD<sub>PilP-loop</sub> from PilP, and  
449 FcpMNO from PilMNO (Extended Data Fig. 1c, 5a, 6b-c, 13b-c). In addition, both PflA  
450 and PflB are similar to another T4P protein, PilF<sup>60</sup>, as all three proteins feature multiple  
451 TPR repeats, though PflA and PflB have additional  $\beta$ -sheets and more TPR repeats than  
452 PilF (Extended Data Fig. 13a).

453

454 Finally, the wide presence of FlgY and potential PflA homologs in flagellated species  
455 of both Terrabacteria (including monoderm and atypical diderm lineages) and Gracilicutes  
456 (including most diderm lineages) suggests that the E-ring and spokes likely have an ancient  
457 origin (Fig. 6c). A recent study suggested that the root of the bacterial phylogenetic tree is  
458 between Terrabacteria and Gracilicutes, and the last bacterial common ancestor was a  
459 flagellated, rod-shaped diderm organism<sup>2</sup>.

460

461

## 462 Discussion

463 As the first discovered rotary nanomachine, the flagellar motor attracted scientists from  
464 diverse disciplines to study its assembly and mechanisms, focusing mainly on the *E. coli*  
465 model. Here, we developed a model for one of the most complex motors in unprecedented  
466 detail, revealing its architecture, assembly, and rotation (Supplementary Video 3). As  
467 accessory scaffolds are not present in the classical model, our work here also provides new

468 mechanisms for motor assembly and function. For example, the early assembly of stator  
469 complexes along with scaffolds in both *C. jejuni* and *B. burgdorferi*<sup>53</sup> contrasts sharply  
470 with the late incorporation of stator complexes in the *E. coli* model<sup>14</sup>. In addition, the lack  
471 of a peptidoglycan layer within the *C. jejuni* motor suggests an activation mechanism  
472 different from that of the *E. coli* model, which depends on the binding of MotB to the  
473 peptidoglycan layer<sup>61</sup>. Furthermore, we showed that the majority of motor structures  
474 imaged by cryo-ET to date have a fixed number of discernable stator complexes and  
475 additional periplasmic scaffolds (Extended Data Fig. 14 and Supplementary Table 1). It is  
476 possible that many species with additional periplasmic scaffolds do not undergo dynamic  
477 exchange of stator complexes or do so with a much lower frequency of exchange than in  
478 the *E. coli* model.  
479

480 The origin and evolution of the flagellum were publicly debated in 2005 due to its  
481 structural complexity, and the exact origin of the flagellum and composition of the ancestral  
482 motor remain elusive<sup>62,63</sup>. Our results suggest that the E-ring and spokes, made of ancient  
483 modules such as ARM and TPR repeats<sup>64,65</sup>, are widely present in modern species and  
484 likely evolved in the motor of the last bacterial common ancestor. Thus, the classical model  
485 with the simplest motor, also a product of horizontal gene transfer, cannot serve as the  
486 prototype of the ancestral motor. Interestingly, the ancestral motor of the phylum  
487 *Campylobacterota* likely recruited part of the T4P structure to generate spokes and cage  
488 units that enclose the stator complexes for flagellar motility (Supplementary Video 4). This  
489 unique evolutionary event provides a good example of exaptation: the recruitment of  
490 elements that initially evolved for other functions in other cellular structures<sup>66</sup>.  
491

492 We recently reported that other accessory proteins and regulators were likely present  
493 in the ancestral motor of the phylum *Campylobacterota*<sup>31</sup>. By contrast, the later, simpler  
494 motor structures in two lineages of this phylum resulted from gene loss or horizontal gene  
495 transfer after loss of the whole ancestral gene set<sup>31</sup>. Therefore, we propose that the  
496 evolution of complex flagellar motors is complicated requiring robust bacterial phylogeny  
497 to track and disentangle. Finally, the evolution of complex motors cannot be attributed  
498 simply to host adaptation, which is biased by studies on bacterial pathogens. For example,  
499 many modern species of *Campylobacterota* have genes that encode all known periplasmic  
500 scaffolds and live in deep-sea hydrothermal vents, on the ocean surface, or in terrestrial  
501 environments<sup>31</sup>. These modern species, including the pathogens *C. jejuni* and *H. pylori*,  
502 likely inherited the ancestral flagellar gene set rather than acquiring scaffolding genes as a  
503 recent adaptation during host association.

504 **Materials and methods**

505 **Bacterial strains and culture conditions**

506 The list of strains, plasmids, and related antibiotics are summarized in Supplementary Table  
507 6 and primers are listed in Supplementary Table 7. The *C. jejuni* 81-176 wild-type (WT)  
508 and mutant strains were routinely grown on blood agar plates (Trypticase soy agar  
509 supplemented with 5% sheep blood) at 37°C in BACTROX-2 microaerobic workstation  
510 (SHELLAB, USA) equilibrated to a 5% O<sub>2</sub> and 10% CO<sub>2</sub> atmosphere. For liquid cultures,  
511 *C. jejuni* strains were grown in Brain Hart Infusion (BHI) medium. The *C. jejuni* mutants  
512 were selected on Brucella broth agar plates supplemented with antibiotics as indicated  
513 below. *E. coli* was grown on LB medium or agar plates at 37°C under aerobic conditions.  
514 The selection medium contained antibiotics at the following concentrations:  
515 chloramphenicol: 50 µg ml<sup>-1</sup> for *E. coli* and 10 µg ml<sup>-1</sup> for *C. jejuni*; kanamycin: 50 µg ml<sup>-1</sup>  
516 ; apramycin: 50 µg ml<sup>-1</sup>; ampicillin: 100 µg ml<sup>-1</sup>. All *C. jejuni* strains were stored at -80°C  
517 in BHI medium with 30% glycerol, and *E. coli* strains were stored at -80°C in LB medium  
518 with 15% glycerol.

519

520 ***C. jejuni* mutant construction and complementation**

521 *C. jejuni* knockout mutant strains were constructed by the gene insertion or replacement  
522 strategy, in which an antibiotic resistance cassette was inserted into the open reading frame  
523 (ORF) of the target gene as previously described<sup>67</sup>. The upstream and downstream regions  
524 of the target gene (approximately 1 kb each fragment) were PCR amplified and introduced  
525 a BamHI or EcoRI restriction enzyme cutting site in the middle. The two fragments were  
526 fused into the linearized pBluescript II SK plasmid following the Gibson assembly protocol  
527<sup>68</sup>. The resulting plasmid was digested with BamHI or EcoRI enzyme, then a kanamycin or  
528 apramycin gene cassette was inserted by T4 ligase. The recombination plasmids were  
529 transformed to *E. coli* DH5α and transformants were selected on LB plates containing  
530 kanamycin or apramycin. All plasmids were verified by DNA sequencing and were  
531 naturally transformed into *C. jejuni* for gene allelic exchange. The transformants were  
532 selected on Brucella broth agar plates with kanamycin or apramycin. The mutation was  
533 confirmed by PCR analysis and DNA sequencing.

534

535 The *C. jejuni* gene knockout mutants were complemented by inserting the wild-type  
536 copy of the target gene into the *hsdR* locus with a chloramphenicol resistance cassette and  
537 a 3×FLAG tag fused to the target gene as previously described<sup>33</sup>. The complemented  
538 mutants were selected on Brucella broth agar plates with chloramphenicol and  
539 kanamycin/apramycin. PCR tests were used to verify the recombinant gene regions of all  
540 constructs.

541

542 **Soft agar motility assay**

543 The *C. jejuni* strains were incubated on blood agar plates for 24 h under microaerobic  
544 conditions at 37°C. A sterilized tip was used to dip into the colony, which was then stabbed

545 into semisolid Brucella broth plates with 0.3% agar. The plates were incubated  
546 microaerobically (85% N<sub>2</sub>, 10% CO<sub>2</sub>, 5% O<sub>2</sub>) at 37°C for 20-36 h.  
547

#### 548 **Immunoprecipitation of interacting proteins and LC-MS/MS analysis**

549 *C. jejuni* strains expressing a 3×FLAG-tagged version of the different proteins were grown  
550 on blood agar, resuspended in phosphate-buffer saline (PBS), pelleted at 6,000 rpm, and  
551 then resuspended in 2 ml of Tris-buffered saline (TBS), 1% Triton X-100, and 0.5 mM  
552 MgSO<sub>4</sub> containing protease inhibitors and 10 µg ml<sup>-1</sup> DNase. After lysis by sonication, cell  
553 debris were removed by centrifugation at 14,000 rpm, supernatants were recovered, and  
554 immunoprecipitation (IP) of 3×FLAG-bait protein was performed using anti-FLAG M2  
555 affinity gel following the manufacturer recommendations. Bound proteins were eluted  
556 twice by acid elution with 40 µl of 0.1 M glycine-HCl buffer at pH 3.5. All the elution  
557 products were pooled and loaded onto a 10% SDS-PAGE gel for LC-MS/MS. The  
558 identification of IP products by LC-MS/MS was conducted as previously described<sup>69</sup>.  
559

#### 560 **Cryo-ET sample preparation**

561 *C. jejuni* strains were streaked on Tryptic Soy Agar (TSA) plate and grown at 37°C for  
562 overnight. Then, bacteria were harvested and inoculated into BHI broth to grow at 37°C  
563 for 5 h. To grow bacteria under microaerobic condition, bacterial plate and cultures were  
564 put in a jar with CampyGen™ 2.5L (Thermo Fisher Scientific). 50 µg ml<sup>-1</sup> of kanamycin  
565 was added into TSA plate and BHI medium to grow all mutant strains. For cryo-ET sample  
566 preparation, bacterial pellets were prepared by centrifugation with 1,500 ×g for 10 min and  
567 resuspended with PBS to a final OD<sub>600</sub> of 1.0. BSA coated gold tracer solution with 10 nm  
568 particle size (Aurion) was then added to the bacterial resuspension at a ratio of 1:1 (V/V).  
569 5 µl of the mixture was deposited on the carbon side of discharged cryo-EM grids  
570 (Quantifoil, Cu) at room temperature. Filter paper (Whatman™) was used to blot on the  
571 backs of grids for almost 4 s, and cryo-EM grids were immediately plunged into liquid  
572 ethane and propane mixture using a manual gravity plunger as described previously<sup>27</sup>. EM  
573 GP2 plunger (Leica) was also used to prepare cryo-EM samples. Briefly, GP2  
574 environmental chambers were set to 25°C and 95% humidity. 5 µl of the mixture were  
575 applied to the carbon side of the discharged cryo-EM grids (Quantifoil, Cu). The grids were  
576 then blotted for 6 s and immediately plunge frozen in the liquid ethane and propane mixture.  
577

#### 578 **Cryo-ET data collection**

579 Frozen-hydrated specimens of *C. jejuni* were imaged below -180°C using Titan Krios G2  
580 300 kV transmission electron microscope (Thermo Fisher Scientific) equipped with a field  
581 emission gun, K3 direct detection camera (Gatan), and GIF BioQuantum imaging Filter  
582 (Gatan). The low-dose mode in SerialEM software<sup>70</sup> was used to record tilt series images  
583 at 42,000× magnification with a physical pixel size of 2.148 Å. The tilt series images from  
584 Δ*rpoN* mutant were recorded below -180°C using Glacios 200 kV transmission electron  
585 microscope (Thermo Fisher Scientific) equipped with a field emission gun with K3 direct

586 detector (Gatan). The images were recorded at 17,500 $\times$  magnification with a physical pixel  
587 size of 2.466 Å using SerialEM software<sup>70</sup>. The angle of the tilt series ranged from -48° to  
588 +48° in increments of 3°, and the stage was tilted with the dose-symmetric scheme in  
589 FastTomo script<sup>71</sup>. The total accumulated electron dose was ~65e<sup>-</sup>/Å<sup>2</sup> distributed across 33  
590 images in the tilt series, and 10 frames of each image were recorded using the dose fraction  
591 mode in SerialEM. Parameters of cryo-ET data aquation were summarized in  
592 Supplementary Table 8.

593

#### 594 **Cryo-ET data analysis**

595 MotionCor2<sup>72</sup> was used to correct the image drifting induced by the electron beam during  
596 the data aquation. Then, IMOD software was used to create image stacks and align all  
597 images in each tilt series by tracking with the 10 nm fiducial bead<sup>73,74</sup>. For this tilt series  
598 alignment step, almost 10 fiducial beads in each image were tracked across the tilt series.  
599 For tilt series with nonsufficient numbers of fiducial beads, the patch tracking in IMOD  
600 was used for the alignment. Gctf<sup>75</sup> was used to estimate defocus for all images in the  
601 aligned tilt series, and contrast transfer function (CTF) was corrected using the ctfphaseflip  
602 function in IMOD<sup>76</sup>. The binvol function in IMOD was used to generate 6 $\times$  binning of the  
603 aligned stacks. 6 $\times$  binned tomograms with Simultaneous Iterative Reconstruction  
604 Technique (SIRT) were reconstructed for the particle picking, and tomograms with  
605 weighted back projection (WBP) were reconstructed for the subtomogram averaging. Both  
606 SIRT and WBP reconstruction was done by Tomo3D<sup>77</sup>. In total, 1,601 tomograms were  
607 analyzed (Supplementary Table 8).

608

#### 609 **In-situ flagellar motor structure analysis by subtomogram averaging**

610 Flagellar motors at the bacterial pole region were manually picked using the tomopick  
611 command in i3 software package<sup>78-80</sup>, and the total numbers of flagellar motors for the  
612 subtomogram averaging are shown in Supplementary Table 8. I3 software package was  
613 used to align particles and determine subtomogram averaged structure in 6 $\times$  binned  
614 tomograms. For further structural analysis, subtomograms were extracted based on the  
615 aligned positions of flagellar motors in the 6 $\times$  binned tomograms. Then, 2 $\times$  and 4 $\times$  binned  
616 subtomograms were generated using the binvol function in IMOD. The 3D classification  
617 was performed to remove bad particles and determine C17 symmetrical structures in  
618 averaged structures that were used for the refinement. The C17-symmetry expansion was  
619 applied for averaged structures in 4 $\times$  binned subtomograms to increase the particle  
620 numbers of flagellar motors. Then, averaged structures were refined using the 2 $\times$  binned  
621 subtomograms. For the focused refined structures, local areas of the motor structures in un-  
622 binned subtomograms were extracted and refined to determine higher resolution structures.  
623 The resolution was estimated by Fourier Shell Correlation (FSC).

624

#### 625 **Molecular modeling of the *C. jejuni* flagellar motor**

626 The atomic models of FlgY homodimer, PflA and PflB complex, FcpN/FcpO heterodimer,

627 and FliL ring were predicted by AlphaFold3<sup>81</sup>. For the PflA and PflB complex, the  
628 predicted structure was used as template, and then the N-terminal domain of PflA and PflB  
629 were replaced with in vitro structure that was determined by single particle analysis of  
630 cryo-EM. Predicted MS-ring, FlgY, PflC, PflD, and FcpMNO complexes were used for the  
631 pseudo-atomic model. For the stator units, the published structure of MotA complex (PDB:  
632 6ykm)<sup>3</sup> and predicted MotB model in *B. burgdorferi* flagellar motor<sup>82</sup> were used for the  
633 modeling. Cryo-EM structures of LP-ring (PDB: 7cbl)<sup>4</sup> and C-ring (PDB: 8uox)<sup>7</sup> were  
634 also used for the modeling. Based on the pseudo-atomic model of *C. jejuni* flagellar motor,  
635 UCSF ChimeraX and Blender were used to create movies based on the cryo-ET analysis  
636 of in situ structures of the motors.  
637

### 638 Protein expression and purification

639 For recombinant protein expression in *E. coli* BL21 (DE3), FlgY and its truncated variants,  
640 as well as PflA<sub>16-788</sub> were cloned into pET22b vector which contains an N-terminal *pelB*  
641 signal peptide for periplasmic targeting and a C-terminal 6×His tag. PflA<sub>16-788</sub> and PflB<sub>113-</sub>  
642 820 were cloned into pET26b, also featuring an N-terminal *pelB* signal peptide for  
643 periplasmic localization but with a C-terminal Strep-tag instead. All constructs were  
644 confirmed by DNA sequencing.  
645

646 *E. coli* BL21 (DE3) carrying plasmids encoding FlgY and its truncation variants and  
647 PflA<sub>16-788</sub>-Strep construct were grown in 1 L LB medium and induced with 0.2 mM  
648 isopropyl-β-d-thiogalactopyranoside (IPTG) at OD<sub>600</sub> of ~0.8. After growing for 16 h at  
649 20°C, the cell was harvested and resuspended in high salt lysis buffer (20 mM Tris-HCl  
650 buffer at pH 8.0 and 500 mM NaCl) and lysed by high-pressure cell crusher (Union-  
651 Biotech). The lysates were centrifuged at 17,000 ×g for 50 min and the supernatants were  
652 loaded onto Ni-NTA resin (Qiagen) or Strep-affinity beads (IBA Lifesciences). After  
653 washing with high salt lysis buffer, the proteins were eluted with 250 mM imidazole and  
654 further purified by gel filtration chromatography (Superdex 200 Increase 10/300 GL, GE  
655 Healthcare) with lysis buffer (20 mM Tris-HCl buffer at pH 8.0 and 300 mM NaCl).  
656

657 For PflA<sub>16-788</sub> and PflB<sub>113-820</sub> complex protein purification, the growth medium was  
658 changed from LB to TB and the lysis buffer composition was adjusted to include 300 mM  
659 NaCl. All other purification steps remained unchanged. For MST experiments, all buffers  
660 were replaced with HEPES buffer at pH 7.5.  
661

### 662 Cryo-EM sample preparation and data collection

663 Aliquots of 4 μl of the PflA<sub>16-788</sub> and PflB<sub>113-820</sub> complex, at a concentration of 0.4 mg ml<sup>-1</sup>,  
664 were applied onto glow-discharged holey Quantifoil carbon-coated grids (Cu R1.2/1.3,  
665 300 mesh, Beijing Zhongjingkeyi Technology, Beijing, China). Following a 5 s incubation  
666 on the grids under 100% humidity, the grids were blotted for 3 s at 8 °C using a blot force  
667 of 1, and then plunged into liquid ethane using a Vitrobot Mark IV (Thermo Fisher

668 Scientific). EPU software (Thermo Fisher Scientific) was employed for automated data  
669 collection on a Glacios 2 transmission electron microscope equipped with an energy filter.  
670 The data were collected using a Falcon4i camera in super-resolution mode, with a defocus  
671 range of -0.5 to -1.5  $\mu\text{m}$  and at a nominal magnification of 130,000 $\times$  (resulting a calibrated  
672 physical pixel size of 0.89  $\text{\AA}$ ). The accumulated dose was set to 40 electrons per  $\text{\AA}^2$ . Data  
673 acquisition parameters, including exposure time, beam intensity, and drift correction  
674 settings, are detailed in Supplementary Table 9.

675

### 676 **Cryo-EM image processing**

677 A total of 5,055 micrographs were acquired and imported into cryoSPARC <sup>83</sup>. Drift  
678 correction and dose-weighting were conducted using MotionCor2 <sup>72</sup>. CTF parameters were  
679 estimated using CTF Estimation (CTFFIND4) in cryoSPARC <sup>83</sup>. Subsequently, 1,265,294  
680 particles were auto picked and extracted from 4,661 micrographs with a box size of 320  
681 pixels for 3 rounds of 2D classification, after this cleaning step, only 161,182 particles  
682 remained for further analysis. All extracted particles were utilized for 3D classification.  
683 These particles were classified into four classes after ab-initio reconstruction and  
684 heterogeneous refinement and NU refinement, resulting in a structure at 3.55  $\text{\AA}$  resolution.  
685

686 To further improve the resolution, we referred to a “seed” strategy <sup>84</sup>, the raw particles  
687 were divided into 6 subgroups and combined with the “seed” particles, which was the NU  
688 refinement result. The combined particle subsets were subjected to multiple rounds of  
689 guided multi-reference 3D classification. After the optimized procedure for data processing,  
690 the dataset of PflA<sub>16-163</sub> and PflB<sub>113-820</sub> gave rise to the final structure at 3.23  $\text{\AA}$  resolution.  
691 A flowchart showing the data processing is shown in Extended Data Fig. 4.  
692

### 693 **Model building, refinement, and visualization**

694 The initial model of PflA<sub>16-163</sub> and PflB<sub>178-820</sub> complex was built by Cryo-Net sever <sup>85</sup>, and  
695 manually adjusted in Coot <sup>86</sup>. Model refinement was performed using  
696 *phenix.real\_space\_refine* tool within Phenix <sup>87</sup>. Cryo-EM structure and model were  
697 visualized by using PyMOL and ChimeraX. The refinement statistics are summarized in  
698 Supplementary Table 9.

699

### 700 **Microscale thermophoresis (MST) binding assay**

701 MST measurements were conducted on a Monolith NT.115 (NanoTemper) with 20% LED  
702 power and 40% MST power. Purified proteins (FlgY<sub>15-172</sub>/ FlgY<sub>90-172</sub>) were diluted at a  
703 concentration of 200 nM in the MST buffer containing PBS and 0.05% (w/v) Tween-20.  
704 PflA<sub>16-788</sub>-Strep protein was titrated from 0 to 60  $\mu\text{M}$ , and then the samples were loaded  
705 into MST NT.115 standard glass capillaries for measurements. Data represent mean  $\pm$  SEM  
706 of three independent measurements.  
707

### 708 **Protein cross-linking**

709 Purified FlgY<sub>15-172</sub>/ FlgY<sub>90-172</sub> protein was diluted to a final concentration of 25 μM in  
710 HEPES buffer (20mM HEPES buffer at pH 7.5, 300 mM NaCl). The mixture was incubated  
711 with EGS to a final concentration of 1 mM, dissolved in anhydrous DMSO, for 30, 60 or  
712 90 min at room temperature. The DMSO concentration was consistently maintained at 1%  
713 (V/V) of the total reaction volume. Reactions were terminated by adding 2 μl 1 M Tris-  
714 HCl buffer at pH 8.0, followed by mixing for 5 min at room temperature. Samples were  
715 subsequently boiled for 5 min and subjected to 15% SDS-PAGE analysis.

716

### 717 **Bacterial two hybrid (BTH) analysis**

718 The assays were performed as described to investigate protein-protein interactions <sup>88</sup>.  
719 Proteins of interest were fused to T25 or T18 fragments in plasmids pKNT25/pKT25 or  
720 pCH363/pUT18C (Supplementary Table 6). The pair of plasmids expressing fusion  
721 proteins with T18 or T25 fragments was co-transformed into *E. coli* strain BTH101 and  
722 plated on LB agar containing ampicillin (100 μg ml<sup>-1</sup>) and kanamycin (50 μg ml<sup>-1</sup>).  
723 Multiple transformants were inoculated into individual tubes with 0.5 ml of LB broth  
724 containing the same antibiotics and 0.5 mM IPTG. The cultures were incubated for 8 h at  
725 30°C with shaking. Two microliters of each culture were spotted on LB plates containing  
726 the antibiotics, 40 μg ml<sup>-1</sup> X-Gal, and 0.5 mM IPTG. The plates were incubated at 30 °C  
727 for 24 h.

728

### 729 **RNA extraction, RNA-seq, and quantitative real-time PCR**

730 *C. jejuni* wild-type and Δ*rpoN*, Δ*fliA* mutants were grown separately under microaerobic  
731 conditions and harvested during the mid-exponential phase. RNA was extracted using a  
732 TIANamp RNAPrep Pure Cell/Bacteria Kit. The purity and concentration of the RNA were  
733 determined by gel electrophoresis and a NanoDrop spectrophotometer (Thermo Fisher  
734 Scientific). Samples were submitted to GENEWIZ (Suzhou, China) for library construction  
735 and sequencing on an Illumina NovaSeq system. The sequencing reads were mapped to the  
736 *C. jejuni* 81-176 genome using Bowtie2 (v2.2.6). HTSeq (V0.6.1) was used to count the  
737 read numbers mapped to each gene, and then the FPKM (Fragments Per Kilo bases per  
738 Million reads) of each gene was calculated. Differential expression analysis of mutant vs.  
739 wild type was performed using the DESeq2 (V1.26.0).

740

741 For qRT-PCR analyses, total RNA was extracted as described above, followed by  
742 DNase I treatment. Then RNA was transcribed using the cDNA Master Kit (TOYOBO,  
743 Japan). Transcript levels were determined with SYBR Green Realtime PCR Master Mix  
744 (TOYOBO, Japan) in a CFX96 Connect Real-Time PCR Detection System (Bio-Rad). The  
745 cycling parameters were 95 °C for 30 s, followed by 40 cycles of 94 °C for 15 s and 60 °C  
746 for 30 s. The abundance of the *rpsQ* gene was used as an internal standard, and the relative  
747 expression levels of genes of interest were calculated using the Quantitation-Comparative  
748 CT (2-ΔΔCT) method <sup>89</sup>.

749

750 **Bioinformatics analysis of flagellar inner-membrane proximal scaffolding proteins  
751 and T4P components in the phylum *Campylobacterota***

752 The genomes of 82 representative species of the phylum *Campylobacterota* from our  
753 previous study<sup>31</sup> were analyzed for homologs of seven flagellar scaffolding proteins (FlgY,  
754 PflA, PflB, PflD, FcpM, FcpN, and FcpO). The sequences of these proteins from *C. jejuni*  
755 81-176 were used as queries for local BLAST search, and the best hit with an E-value <  
756 1e<sup>-3</sup> as potential homologs. Then, structural similarity of candidate homologs was  
757 confirmed using HHpred<sup>90</sup> and AlphaFold3<sup>81</sup>. All identified protein homologs are  
758 summarized in Supplementary Table 4.

759

760 To identify T4P components, MacSyFinder<sup>91</sup> was first used to identify a complete T4P  
761 gene cluster in *Campylobacter sputorum* genome (NCBI accession number:  
762 GCF\_002220775.1). Then, nine core T4P components (PilM, PilN, PilO, PilP, PilQ, PilB,  
763 PilC, PilT, and PilU) from *C. sputorum* were used as queries for local BLAST searches  
764 against 82 *Campylobacterota* genomes to identify potential candidate homologs (E-value  
765 < 1e<sup>-5</sup>). The candidate proteins were further analyzed for domain organization using the  
766 SMART database<sup>92</sup> and for structural similarity using HHpred<sup>90</sup> and AlphaFold3<sup>81</sup>. Since  
767 T4P belongs to type IV filament (TFF) superfamily and its components share homology  
768 with other TFF systems<sup>93</sup>, manual curation was performed to verify that the identified  
769 clusters belong to T4P rather than the other TFF systems. For manual curation, the  
770 identified clusters and their neighborhood genes (five genes upstream and downstream)  
771 were examined for the presence of characteristic proteins from other TFF systems based  
772 on reference<sup>93</sup>. All identified T4P components are summarized in Supplementary Table 4.  
773

774

775 To study the evolution of flagellar scaffolding proteins and T4P in *Campylobacterota*,  
776 the above identified homologs were mapped onto a species tree that also includes  
777 flagellation status and chemosensory classes of each species based on data from our recent  
778 studies<sup>31</sup>. Briefly, the species tree was constructed using the UBCG pipeline<sup>94</sup>, based on  
779 the sequence alignment of 92 single-copy concatenated marker proteins derived from the  
780 complete genomes of 82 *Campylobacterota* species<sup>31</sup>. Six closely related *Desulfurellales*  
species were included as an outgroup to root the tree<sup>31</sup>.

781

782 **Bioinformatics analysis of flagellar inner-membrane proximal scaffolding proteins in  
783 the *Bacteria* domain**

784 Genomes of representative species, totaling 16,533, were downloaded from NCBI on April  
785 3, 2023 ([https://www.ncbi.nlm.nih.gov/datasets/genome/?taxon=2&reference\\_only=true](https://www.ncbi.nlm.nih.gov/datasets/genome/?taxon=2&reference_only=true)).  
786 To address the considerable variation in the number of representative species across  
787 different taxa and ensure balanced species counts, the following criteria were applied: (1).  
788 for large groups or subgroups with more than 200 genomes, only complete genomes were  
789 selected and if the number of complete genomes exceeded 200, only one genome per genus  
790 was retained; (2). for smaller groups or subgroups with fewer than 200 genomes, all

791 genomes were kept to ensure species diversity. Representative species were prioritized  
792 based on experimental characterization, with emphasis on model organisms listed in the  
793 COGs database <sup>95</sup>, especially those whose flagellar motors have been investigated via  
794 Cryo-ET (Supplementary Table 1). Subsequently, CheckM <sup>96</sup> was used to filter genomes  
795 with completeness below 70% or contamination above 10%, resulting in a final dataset of  
796 2,638 genomes. The information of selected 2,638 genomes was listed in Supplementary  
797 Table 5.

798  
799 To determine whether the representative species has flagellar gene set, 24 core flagellar  
800 proteins (FlhA, FlhB, FliP, FliQ, FliR, FliI, FliH, FliF, MotA, MotB, FliG, FliM, FliN, FliE,  
801 FlgB, FlgC, FlgF, FlgG, FlgE, FlgD, FlgK, FlgL, FliC, and FliD) from *S. enterica* or  
802 *Bacillus subtilis* were used as queries for both BLASTP and PSI-BLAST searches <sup>97</sup>.  
803 Given the presence of incomplete genomes and pseudogenes, species with at least 20 core  
804 genes were classified as possessing flagellar gene set. Consequently, 1,365 species were  
805 identified as “flagellated species” (species with flagellar gene set) and used for further  
806 phylogenetic analysis and homolog searches. A maximum likelihood (ML) phylogenetic  
807 tree was constructed for these 1,365 species using 120 markers from GTDB-Tk v2 <sup>98</sup>, with  
808 the concatenated multiple sequence alignment applied to infer the tree with IQ-TREE <sup>99</sup>.  
809 The best fit model, LG+R10, was selected by ModelFinder, and bootstrap was estimated  
810 based on 1,000 replications. Phylogenetic tree was visualized, annotated, and modified  
811 using iTOL v6 <sup>100</sup>.

812  
813 To identify FlgY homologs, comprehensive HMM homology searches <sup>101</sup> were  
814 performed following this strategy: (1). The MgtE\_N Hidden Markov Model (HMM)  
815 profile (Pfam PF03448) was used to search against 1,365 flagellated species; (2). the hits  
816 obtained from the HMM search were further validated by structural analyses including  
817 SMART database <sup>92</sup>, HHpred <sup>90</sup> and AlphaFold3 <sup>81</sup>, but only if they were located within  
818 five genes adjacent to the flagellar gene clusters; (3) to find homologs overlooked by the  
819 HMM search, genes neighboring *fliJ* or *fliK* were also examined using SMART database,  
820 HHpred or AlphaFold3.

821  
822 PflA and PflB homologs are not conserved either in sequence level or in gene order  
823 across different taxa. For some taxa with experimentally investigated homologs, these  
824 homologs were used as queries for BLAST search against the specific taxon. For example,  
825 PflAB from *C. jejuni* <sup>33</sup> were used as queries for both BLASTP and PSI-BLAST searches  
826 against *Campylobacterota*; FlcAB from *B. burgdorferi* were used for searches against  
827 *Spirochaetota* <sup>18,25</sup>; and MotC from *S. meliloti* <sup>58</sup>, MotK from *C. sphaeroides* <sup>59</sup>, and  
828 CC\_2058 from *C. crescentus* were used for searches against α-proteobacteria. For other  
829 taxa, extensive HMM homology searches were carried out according to the following  
830 criteria: (1). The TPR HMM profile (Pfam PF00515) was applied to search against the  
831 genomes of flagellated species with FlgY homologs; (2). the hits retrieved from the HMM

832 search were further confirmed using TPRpred<sup>102</sup> and SMART database, but only if they  
833 were located within five genes adjacent to the flagellar gene clusters; (3). as TPR repeats  
834 typically consist of more than 3 consecutive motifs<sup>103</sup>, candidates with less than 3  
835 sequential motifs were discarded; (4). candidates containing functional known domains  
836 that are enriched in TPR repeats, such as glycosyltransferase, methyltransferases,  
837 acetyltransferase, sulfotransferase, metalloprotease, were further excluded.

838

839 PfID exhibits considerable sequence variability in its N-terminal loop region and its  
840 C-terminal domain that shares structural similarity with PilQ-N1 domain has no identified  
841 HMM profile in the Pfam database. Homolog searches of PfID in the phylum  
842 *Campylobacterota* were performed as described above. However, using an HMM profile  
843 built from homologs in *Campylobacterota* could introduce bias for homolog search in other  
844 phyla, thus no further bioinformatics analyses of PfID in the *Bacteria* domain were  
845 performed.

846

847 To identify homologs of cage proteins (FcpM/FcpN/FcpO), the FcpN homologous  
848 protein PilN was selected as a feature protein to locate the *fcpMNO* gene cluster. Sequence  
849 alignment was performed on all PilN proteins (COG3166) in the COG database to construct  
850 an HMM profile. To identify potential candidate homologs in 1,365 flagellated species, an  
851 HMM search was conducted (E-value < 1e<sup>-3</sup>). The candidate proteins were further  
852 examined for domain organization using the SMART database<sup>92</sup> and for structural  
853 similarity using HHpred<sup>90</sup> and AlphaFold3<sup>81</sup>. Additionally, since the genes of cage  
854 proteins are typically clustered together in the genome and not adjacent to any TFF family  
855 genes, gene neighborhood analysis was performed manually to confirm that the identified  
856 gene clusters belonged to *fcpMNO*.

857

858 The structures of FlgY of PflAB homologs in Extended Data Fig. 11 and 12 were  
859 predicted by AlphaFold3<sup>81</sup>. The signal peptides and transmembrane regions were predicted  
860 by SignalP 6.0<sup>104</sup> and TMHMM 2.0<sup>105</sup>, respectively. All identified proteins are  
861 summarized in Supplementary Table 5.

862 **Acknowledgments:**

863 The authors would like to thank Drs. Brian Crane and Michael Lynch from Cornell  
864 University for discussion of the ARM-like domain; the High-Performance Computing  
865 Division at the South China Sea Institute of Oceanology for data analysis; Jennifer Aronson  
866 (Yale University) for editing and valuable comments on the manuscript; Yale Center for  
867 Research Computing (YCRC) for guidance and use of the research computing  
868 infrastructure; Xiaoju Li, Jing Zhu, and Zhifeng Li from Shandong University Core  
869 Facilities for Life and Environmental Sciences for their help with the Cryo- EM and MST  
870 experiments.

871

872 **Funding:**

873 This research was supported by the National Natural Science Foundation of China  
874 (32470031 and 32370189), National Key Research and Development Program of China  
875 (2022YFC3102003), the Science and Technology Planning Project of Guangdong Province  
876 of China (2021B1212050023), and Innovation Academy of South China Sea Ecology and  
877 Environmental Engineering, Chinese Academy of Sciences (NO. ISEE2021ZD03 and  
878 ISEE2021PY05). J. H. and X.G. were supported by Shandong Provincial Natural Science  
879 Foundation (ZR2024ZD47) and SKLMT Frontiers and Challenges Project (SKLMTFCP-  
880 2023-01). S.T. J.M.B. and J.L. were supported by grants R01AI087946 and R01AI132818  
881 from the National Institute of Allergy and Infectious Diseases (NIAID); cryo-ET data were  
882 collected at Yale CryoEM Resource, which was funded in part by the NIH grant  
883 1S10OD023603-01A1. H.Z. was supported by funds from the State Key Laboratory of  
884 Crop Stress Adaptation and Improvement of Henan University.

885

886 **Author Contributions**

887 B.G. and J.L. conceived and designed the study. Genetic, protein interaction, RNA-seq and  
888 partial biochemical experiments were performed by X.F. with assistance from Y.L., Y.C.  
889 and M.A.B. Cryo-ET experiments and related structural analyses were performed by S.T.  
890 with assistance from H.Z. and C.H., and modeling was performed by J.M.B and S.T. Single  
891 particle cryo-EM experiments of PflAB and biochemical analyses of FlgY were performed  
892 by J.H. under the supervision of X.G. Phylogenetic analysis and homolog search were  
893 performed by S.Z. with assistance from Y.L. Partial mutants were provided by C.H. and  
894 M.L.T., and LC-MS/MS experiments were performed by M.L.T. The manuscript was  
895 written by B.G., J.L., S.T. and X.F. All authors contributed to editing the manuscript, and  
896 support the conclusions.

897

898 **Data Availability Statement:** All relevant data are within the manuscript and its  
899 Supporting Information files. The cryo-ET maps of the motor in wild-type *C. jejuni*, and  
900  $\Delta motA$ ,  $\Delta flgY$ ,  $\Delta pflA$ ,  $\Delta pflB$ ,  $\Delta pflC$ ,  $\Delta pflD$ , and  $\Delta fcpMNO$  mutant cells have been deposited  
901 in the Electron Microscopy Data Bank under accession codes EMD-45507, EMD-45508,  
902 EMD-49254, EMD-49256, EMD-49255, EMD-49253, EMD-49252, respectively. The

903 cryo-EM map and atomic coordinates have been deposited in the Protein Data Bank and  
904 the Electron Microscopy Data Bank under the accession numbers 9LEQ and EMD-63032,  
905 respectively. Further details are provided in Supplementary Table 8 and 9. Raw reads of  
906 RNA-seq studies have been deposited in the Sequence Read Archive  
907 (<https://www.ncbi.nlm.nih.gov/sra>) under BioProject numbers PRJNA1223640. The  
908 transcriptome datasets generated in this study are summarized in Supplementary Table 3.  
909 The *Campylobacter jejuni* 81-176 reference genome (NCBI accession number:  
910 GCA\_000015525.1) is available for download from NCBI  
911 ([https://ftp.ncbi.nlm.nih.gov/genomes/all/GCF/000/015/525/GCF\\_000015525.1\\_ASM15](https://ftp.ncbi.nlm.nih.gov/genomes/all/GCF/000/015/525/GCF_000015525.1_ASM15)  
912 52v1/).

913

914

## 915 References

916

- 917 1 Wadhwa, N. & Berg, H. C. Bacterial motility: machinery and mechanisms. *Nature reviews. Microbiology* **20**, 161-173 (2022). <https://doi.org/10.1038/s41579-021-00626-4>
- 918 2 Coleman, G. A. *et al.* A rooted phylogeny resolves early bacterial evolution. *Science* **372** (2021). <https://doi.org/10.1126/science.abe0511>
- 919 3 Santiveri, M. *et al.* Structure and Function of Stator Units of the Bacterial Flagellar Motor. *Cell* **183**, 244-257 e216 (2020). <https://doi.org/10.1016/j.cell.2020.08.016>
- 920 4 Tan, J. *et al.* Structural basis of assembly and torque transmission of the bacterial flagellar motor. *Cell* **184**, 2665-2679 e2619 (2021). <https://doi.org/10.1016/j.cell.2021.03.057>
- 921 5 Kreutzberger, M. A. B. *et al.* Convergent evolution in the supercoiling of prokaryotic flagellar filaments. *Cell* **185**, 3487-3500 e3414 (2022). <https://doi.org/10.1016/j.cell.2022.08.009>
- 922 6 Johnson, S. *et al.* Molecular structure of the intact bacterial flagellar basal body. *Nat Microbiol* **6**, 712-721 (2021). <https://doi.org/10.1038/s41564-021-00895-y>
- 923 7 Johnson, S. *et al.* Structural basis of directional switching by the bacterial flagellum. *Nat Microbiol* (2024). <https://doi.org/10.1038/s41564-024-01630-z>
- 924 8 Chen, S. *et al.* Structural diversity of bacterial flagellar motors. *The EMBO journal* **30**, 2972-2981 (2011). <https://doi.org/10.1038/emboj.2011.186>
- 925 9 Beeby, M. *et al.* Diverse high-torque bacterial flagellar motors assemble wider stator rings using a conserved protein scaffold. *Proceedings of the National Academy of Sciences of the United States of America* **113**, E1917-1926 (2016). <https://doi.org/10.1073/pnas.1518952113>
- 926 10 Zhu, S. *et al.* Molecular architecture of the sheathed polar flagellum in *Vibrio alginolyticus*. *Proceedings of the National Academy of Sciences of the United States of America* **114**, 10966-10971 (2017). <https://doi.org/10.1073/pnas.1712489114>
- 927 11 Kaplan, M. *et al.* The presence and absence of periplasmic rings in bacterial flagellar motors correlates with stator type. *eLife* **8** (2019). <https://doi.org/10.7554/eLife.43487>
- 928 12 Zhu, S. *et al.* In Situ Structures of Polar and Lateral Flagella Revealed by Cryo-Electron Tomography. *Journal of bacteriology* **201** (2019). <https://doi.org/10.1128/JB.00117-19>
- 929 13 Rossmann, F. M. & Beeby, M. Insights into the evolution of bacterial flagellar motors from

- 944                          high-throughput *in situ* electron cryotomography and subtomogram averaging. *Acta*  
945                          *Crystallogr D Struct Biol* **74**, 585-594 (2018). <https://doi.org/10.1107/S2059798318007945>
- 946                          14 Armitage, J. P. & Berry, R. M. Assembly and Dynamics of the Bacterial Flagellum. *Annu Rev*  
947                          *Microbiol* **74**, 181-200 (2020). <https://doi.org/10.1146/annurev-micro-090816-093411>
- 948                          15 Hu, H. *et al.* Structural basis of torque generation in the bi-directional bacterial flagellar motor.  
949                          *Trends Biochem Sci* **47**, 160-172 (2022). <https://doi.org/10.1016/j.tibs.2021.06.005>
- 950                          16 Leake, M. C. *et al.* Stoichiometry and turnover in single, functioning membrane protein  
951                          complexes. *Nature* **443**, 355-358 (2006). <https://doi.org/10.1038/nature05135>
- 952                          17 Ferreira, J. L. *et al.* The "Jack-of-all-Trades" Flagellum From *Salmonella* and *E. coli* Was  
953                          Horizontally Acquired From an Ancestral beta-Proteobacterium. *Front Microbiol* **12**, 643180  
954                          (2021). <https://doi.org/10.3389/fmicb.2021.643180>
- 955                          18 Chang, Y., Xu, H., Motaleb, M. A. & Liu, J. Characterization of the Flagellar Collar Reveals  
956                          Structural Plasticity Essential for Spirochete Motility. *mBio* **12**, e0249421 (2021).  
957                          <https://doi.org/10.1128/mBio.02494-21>
- 958                          19 Qin, Z., Lin, W. T., Zhu, S., Franco, A. T. & Liu, J. Imaging the motility and chemotaxis  
959                          machineries in *Helicobacter pylori* by cryo-electron tomography. *Journal of bacteriology* **199**,  
960                          e00695-00616 (2017). <https://doi.org/10.1128/JB.00695-16>
- 961                          20 Zhu, S., Nishikino, T., Kojima, S., Homma, M. & Liu, J. The Vibrio H-Ring Facilitates the Outer  
962                          Membrane Penetration of the Polar Sheathed Flagellum. *Journal of bacteriology* **200** (2018).  
963                          <https://doi.org/10.1128/JB.00387-18>
- 964                          21 Zhou, X. & Roujeinikova, A. The Structure, Composition, and Role of Periplasmic Stator  
965                          Scaffolds in Polar Bacterial Flagellar Motors. *Front Microbiol* **12**, 639490 (2021).  
966                          <https://doi.org/10.3389/fmicb.2021.639490>
- 967                          22 Takekawa, N., Kojima, S. & Homma, M. Mutational analysis and overproduction effects of  
968                          MotX, an essential component for motor function of Na<sup>+</sup>-driven polar flagella of *Vibrio*. *J*  
969                          *Biochem* **161**, 159-166 (2017). <https://doi.org/10.1093/jb/mvw061>
- 970                          23 Moon, K. H. *et al.* Spirochetes flagellar collar protein FlbB has astounding effects in orientation  
971                          of periplasmic flagella, bacterial shape, motility, and assembly of motors in *Borrelia*  
972                          *burgdorferi*. *Molecular microbiology* **102**, 336-348 (2016).  
973                          <https://doi.org/10.1111/mmi.13463>
- 974                          24 Moon, K. H., Zhao, X., Xu, H., Liu, J. & Motaleb, M. A. A tetratricopeptide repeat domain protein  
975                          has profound effects on assembly of periplasmic flagella, morphology and motility of the lyme  
976                          disease spirochete *Borrelia burgdorferi*. *Molecular microbiology* **110**, 634-647 (2018).  
977                          <https://doi.org/10.1111/mmi.14121>
- 978                          25 Xu, H., He, J., Liu, J. & Motaleb, M. A. BB0326 is responsible for the formation of periplasmic  
979                          flagellar collar and assembly of the stator complex in *Borrelia burgdorferi*. *Molecular*  
980                          *microbiology* **113**, 418-429 (2020). <https://doi.org/10.1111/mmi.14428>
- 981                          26 Drobnič, T. *et al.* Molecular model of a bacterial flagellar motor *in situ* reveals a "parts-list" of  
982                          protein adaptations to increase torque. *bioRxiv* (2023).  
983                          <https://doi.org/10.1101/2023.09.08.556779>
- 984                          27 Tachiyama, S. *et al.* The flagellar motor protein FliL forms a scaffold of circumferentially

- 985 positioned rings required for stator activation. *Proceedings of the National Academy of  
986 Sciences of the United States of America* **119** (2022).  
<https://doi.org/10.1073/pnas.2118401119>
- 988 28 San Martin, F., Fule, L., Iraola, G., Buschiazzo, A. & Picardeau, M. Diving into the complexity of  
989 the spirochetal endoflagellum. *Trends in microbiology* **31**, 294-307 (2023).  
<https://doi.org/10.1016/j.tim.2022.09.010>
- 991 29 Snyder, L. A., Loman, N. J., Futterer, K. & Pallen, M. J. Bacterial flagellar diversity and evolution:  
992 seek simplicity and distrust it? *Trends in microbiology* **17**, 1-5 (2009).  
<https://doi.org/10.1016/j.tim.2008.10.002>
- 994 30 Chaban, B., Coleman, I. & Beeby, M. Evolution of higher torque in Campylobacter-type  
995 bacterial flagellar motors. *Sci Rep* **8**, 97 (2018). <https://doi.org/10.1038/s41598-017-18115-1>
- 996 31 Mo, R. *et al.* The evolutionary path of chemosensory and flagellar macromolecular machines  
997 in Campylobacterota. *PLoS genetics* **18**, e1010316 (2022).  
<https://doi.org/10.1371/journal.pgen.1010316>
- 999 32 Lertsethtakarn, P., Ottemann, K. M. & Hendrixson, D. R. Motility and chemotaxis in  
1000 Campylobacter and Helicobacter. *Annu Rev Microbiol* **65**, 389-410 (2011).  
<https://doi.org/10.1146/annurev-micro-090110-102908>
- 1002 33 Gao, B., Lara-Tejero, M., Lefebre, M., Goodman, A. L. & Galan, J. E. Novel components of the  
1003 flagellar system in epsilonproteobacteria. *mBio* **5**, e01349-01314 (2014).  
<https://doi.org/10.1128/mBio.01349-14>
- 1005 34 Hendrixson, D. R. & DiRita, V. J. Identification of *Campylobacter jejuni* genes involved in  
1006 commensal colonization of the chick gastrointestinal tract. *Molecular microbiology* **52**, 471-  
1007 484 (2004). <https://doi.org/10.1111/j.1365-2958.2004.03988.x>
- 1008 35 Sommerlad, S. M. & Hendrixson, D. R. Analysis of the roles of FlgP and FlgQ in flagellar motility  
1009 of *Campylobacter jejuni*. *Journal of bacteriology* **189**, 179-186 (2007).  
<https://doi.org/10.1128/JB.01199-06>
- 1011 36 Ribardo, D. A., Johnson, J. J. & Hendrixson, D. R. Viscosity-dependent determinants of  
1012 *Campylobacter jejuni* impacting the velocity of flagellar motility. *mBio* **15**, e0254423 (2024).  
<https://doi.org/10.1128/mbio.02544-23>
- 1014 37 Gao, B. *et al.* Metabolic and fitness determinants for in vitro growth and intestinal colonization  
1015 of the bacterial pathogen *Campylobacter jejuni*. *PLoS Biol* **15**, e2001390 (2017).  
<https://doi.org/10.1371/journal.pbio.2001390>
- 1017 38 Cohen, E. J. *et al.* Evolution of a large periplasmic disk in Campylobacterota flagella enables  
1018 both efficient motility and autoagglutination. *Dev Cell* **59**, 3306-3321 e3305 (2024).  
<https://doi.org/10.1016/j.devcel.2024.09.008>
- 1020 39 Zamba-Campero, M. *et al.* Broadly conserved FlgV controls flagellar assembly and *Borrelia*  
1021 *burgdorferi* dissemination in mice. *Nat Commun* **15**, 10417 (2024).  
<https://doi.org/10.1038/s41467-024-54806-w>
- 1023 40 Johnson, R. C., Walsh, M. P., Ely, B. & Shapiro, L. Flagellar hook and basal complex of  
1024 *Caulobacter crescentus*. *Journal of bacteriology* **138**, 984-989 (1979).  
<https://doi.org/10.1128/jb.138.3.984-989.1979>

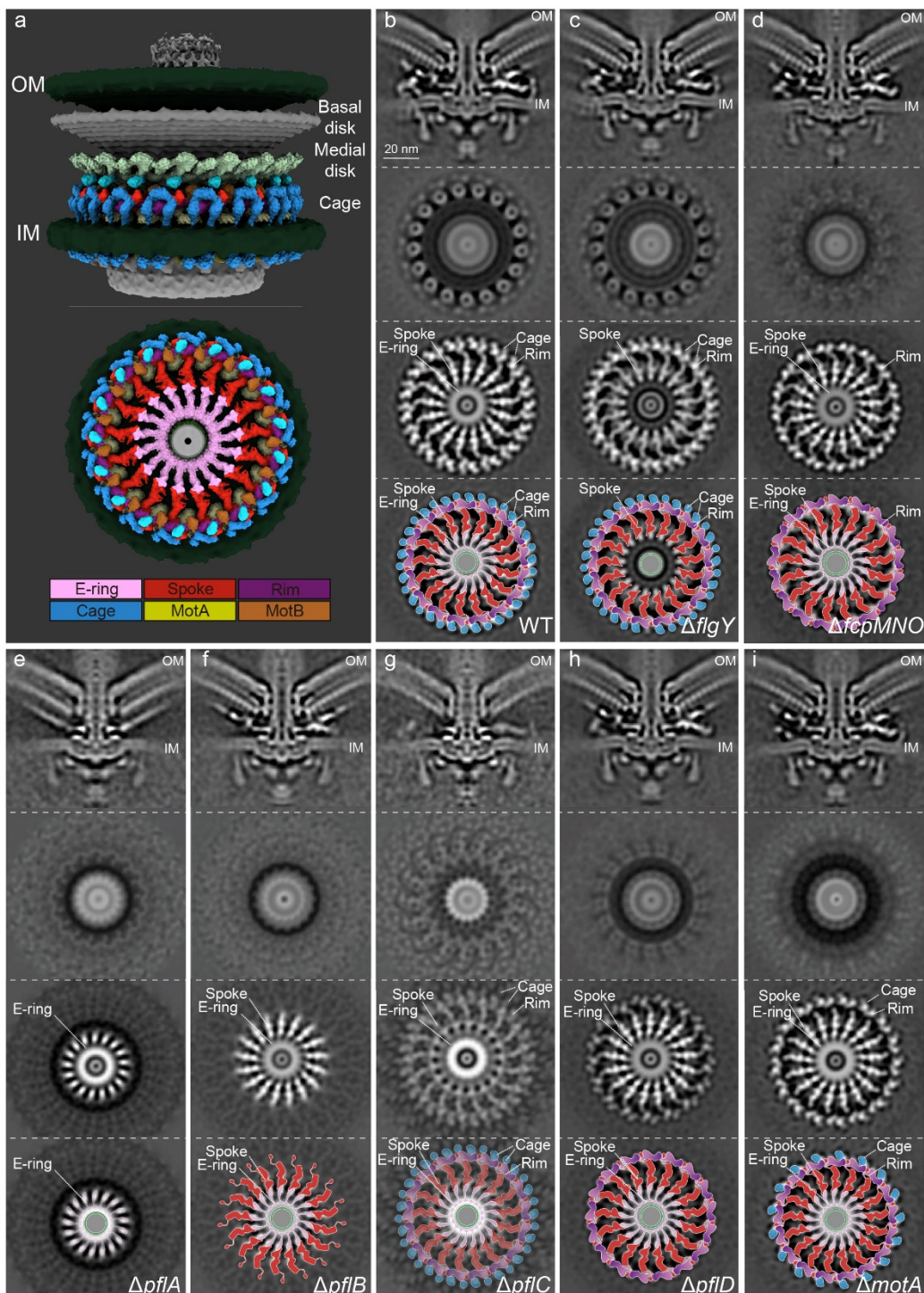
- 1026 41 Stallmeyer, M. J., Hahnenberger, K. M., Sosinsky, G. E., Shapiro, L. & DeRosier, D. J. Image  
1027 reconstruction of the flagellar basal body of *Caulobacter crescentus*. *Journal of molecular*  
1028 *biology* **205**, 511-518 (1989). [https://doi.org/10.1016/0022-2836\(89\)90222-2](https://doi.org/10.1016/0022-2836(89)90222-2)
- 1029 42 Liu, X. *et al.* Bacterial flagella hijack type IV pili proteins to control motility. *Proceedings of the*  
1030 *National Academy of Sciences of the United States of America* **121**, e2317452121 (2024).  
1031 <https://doi.org/10.1073/pnas.2317452121>
- 1032 43 Hattori, M., Tanaka, Y., Fukai, S., Ishitani, R. & Nureki, O. Crystal structure of the MgtE Mg<sup>2+</sup>  
1033 transporter. *Nature* **448**, 1072-1075 (2007). <https://doi.org/10.1038/nature06093>
- 1034 44 Lynch, M. J. *et al.* Co-Folding of a FliF-FliG Split Domain Forms the Basis of the MS:C Ring  
1035 Interface within the Bacterial Flagellar Motor. *Structure* **25**, 317-328 (2017).  
1036 <https://doi.org/10.1016/j.str.2016.12.006>
- 1037 45 Xue, C. *et al.* Crystal structure of the FliF-FliG complex from *Helicobacter pylori* yields insight  
1038 into the assembly of the motor MS-C ring in the bacterial flagellum. *The Journal of biological*  
1039 *chemistry* **293**, 2066-2078 (2018). <https://doi.org/10.1074/jbc.M117.797936>
- 1040 46 Baker, M. A. *et al.* Domain-swap polymerization drives the self-assembly of the bacterial  
1041 flagellar motor. *Nature structural & molecular biology* **23**, 197-203 (2016).  
1042 <https://doi.org/10.1038/nsmb.3172>
- 1043 47 Singh, P. K. *et al.* CryoEM structures reveal how the bacterial flagellum rotates and switches  
1044 direction. *Nat Microbiol* (2024). <https://doi.org/10.1038/s41564-024-01674-1>
- 1045 48 Chen, Y. *et al.* Tetrameric PilZ protein stabilizes stator ring in complex flagellar motor and is  
1046 required for motility in *Campylobacter jejuni*. *Proceedings of the National Academy of*  
1047 *Sciences of the United States of America* **122**, e2412594121 (2025).  
1048 <https://doi.org/10.1073/pnas.2412594121>
- 1049 49 Guo, S. *et al.* PilY1 regulates the dynamic architecture of the type IV pilus machine in  
1050 *Pseudomonas aeruginosa*. *Nat Commun* **15**, 9382 (2024). <https://doi.org/10.1038/s41467-024-53638-y>
- 1052 50 Rocaboy, M. *et al.* The crystal structure of the cell division amidase AmiC reveals the fold of  
1053 the AMIN domain, a new peptidoglycan binding domain. *Molecular microbiology* **90**, 267-  
1054 277 (2013). <https://doi.org/10.1111/mmi.12361>
- 1055 51 McCallum, M., Tamman, S., Rubinstein, J. L., Burrows, L. L. & Howell, P. L. CryoEM map of  
1056 *Pseudomonas aeruginosa* PilQ enables structural characterization of TsaP. *Structure* **29**, 457-  
1057 466 e454 (2021). <https://doi.org/10.1016/j.str.2020.11.019>
- 1058 52 Chevance, F. F. & Hughes, K. T. Coordinating assembly of a bacterial macromolecular machine.  
1059 *Nature reviews. Microbiology* **6**, 455-465 (2008). <https://doi.org/10.1038/nrmicro1887>
- 1060 53 Zhao, X. *et al.* Cryoelectron tomography reveals the sequential assembly of bacterial flagella  
1061 in *Borrelia burgdorferi*. *Proceedings of the National Academy of Sciences of the United States*  
1062 *of America* **110**, 14390-14395 (2013). <https://doi.org/10.1073/pnas.1308306110>
- 1063 54 Jagannathan, A., Constantinidou, C. & Penn, C. W. Roles of rpoN, fliA, and flgR in expression  
1064 of flagella in *Campylobacter jejuni*. *Journal of bacteriology* **183**, 2937-2942 (2001).  
1065 <https://doi.org/10.1128/JB.183.9.2937-2942.2001>
- 1066 55 Kaplan, M. *et al.* Novel transient cytoplasmic rings stabilize assembling bacterial flagellar

- 1067        motors. *The EMBO journal* **41**, e109523 (2022). <https://doi.org/10.15252/embj.2021109523>
- 1068     56        Waite, D. W. *et al.* Comparative Genomic Analysis of the Class Epsilonproteobacteria and  
1069        Proposed Reclassification to Epsilonbacteraeota (phyl. nov.). *Front Microbiol* **8**, 682 (2017).  
1070        <https://doi.org/10.3389/fmicb.2017.00682>
- 1071     57        Zeytuni, N. & Zarivach, R. Structural and functional discussion of the tetra-trico-peptide  
1072        repeat, a protein interaction module. *Structure* **20**, 397-405 (2012).  
1073        <https://doi.org/10.1016/j.str.2012.01.006>
- 1074     58        Eggenhofer, E., Haslbeck, M. & Scharf, B. MotE serves as a new chaperone specific for the  
1075        periplasmic motility protein, MotC, in *Sinorhizobium meliloti*. *Molecular microbiology* **52**,  
1076        701-712 (2004). <https://doi.org/10.1111/j.1365-2958.2004.04022.x>
- 1077     59        Velez-Gonzalez, F. *et al.* Rotation of the Fla2 flagella of *Cereibacter sphaerooides* requires the  
1078        periplasmic proteins MotK and MotE that interact with the flagellar stator protein MotB2. *PLoS  
1079        one* **19**, e0298028 (2024). <https://doi.org/10.1371/journal.pone.0298028>
- 1080     60        Tassinari, M., Rudzite, M., Filloux, A. & Low, H. H. Assembly mechanism of a Tad secretion  
1081        system secretin-pilin complex. *Nat Commun* **14**, 5643 (2023).  
1082        <https://doi.org/10.1038/s41467-023-41200-1>
- 1083     61        Roujeinikova, A. Crystal structure of the cell wall anchor domain of MotB, a stator component  
1084        of the bacterial flagellar motor: implications for peptidoglycan recognition. *Proceedings of  
1085        the National Academy of Sciences of the United States of America* **105**, 10348-10353 (2008).  
1086        <https://doi.org/10.1073/pnas.0803039105>
- 1087     62        Pallen, M. J. & Matzke, N. J. From The Origin of Species to the origin of bacterial flagella.  
1088        *Nature reviews. Microbiology* **4**, 784-790 (2006). <https://doi.org/10.1038/nrmicro1493>
- 1089     63        Egelman, E. H. Reducing irreducible complexity: divergence of quaternary structure and  
1090        function in macromolecular assemblies. *Curr Opin Cell Biol* **22**, 68-74 (2010).  
1091        <https://doi.org/10.1016/j.ceb.2009.11.007>
- 1092     64        Jernigan, K. K. & Bordenstein, S. R. Tandem-repeat protein domains across the tree of life.  
1093        *PeerJ* **3**, e732 (2015). <https://doi.org/10.7717/peerj.732>
- 1094     65        Arrias, P. N. *et al.* Diversity and structural-functional insights of alpha-solenoid proteins.  
1095        *Protein Sci* **33**, e5189 (2024). <https://doi.org/10.1002/pro.5189>
- 1096     66        Gould SJ, V. E. Exaptation—a Missing Term in the Science of Form. *Paleobiology* **8**, 12 (1982).  
1097        <https://doi.org/10.1017/S0094837300004310>
- 1098     67        Cha, G., Chen, Z., Mo, R., Lu, G. & Gao, B. The novel regulators CheP and CheQ control the  
1099        core chemotaxis operon cheVAW in *Campylobacter jejuni*. *Molecular microbiology* **111**, 145-  
1100        158 (2019). <https://doi.org/10.1111/mmi.14144>
- 1101     68        Gibson, D. G. *et al.* Enzymatic assembly of DNA molecules up to several hundred kilobases.  
1102        *Nature methods* **6**, 343-345 (2009). <https://doi.org/10.1038/nmeth.1318>
- 1103     69        Lara-Tejero, M., Kato, J., Wagner, S., Liu, X. & Galan, J. E. A sorting platform determines the  
1104        order of protein secretion in bacterial type III systems. *Science* **331**, 1188-1191 (2011).  
1105        <https://doi.org/10.1126/science.1201476>
- 1106     70        Mastronarde, D. N. Automated electron microscope tomography using robust prediction of  
1107        specimen movements. *J Struct Biol* **152**, 36-51 (2005).

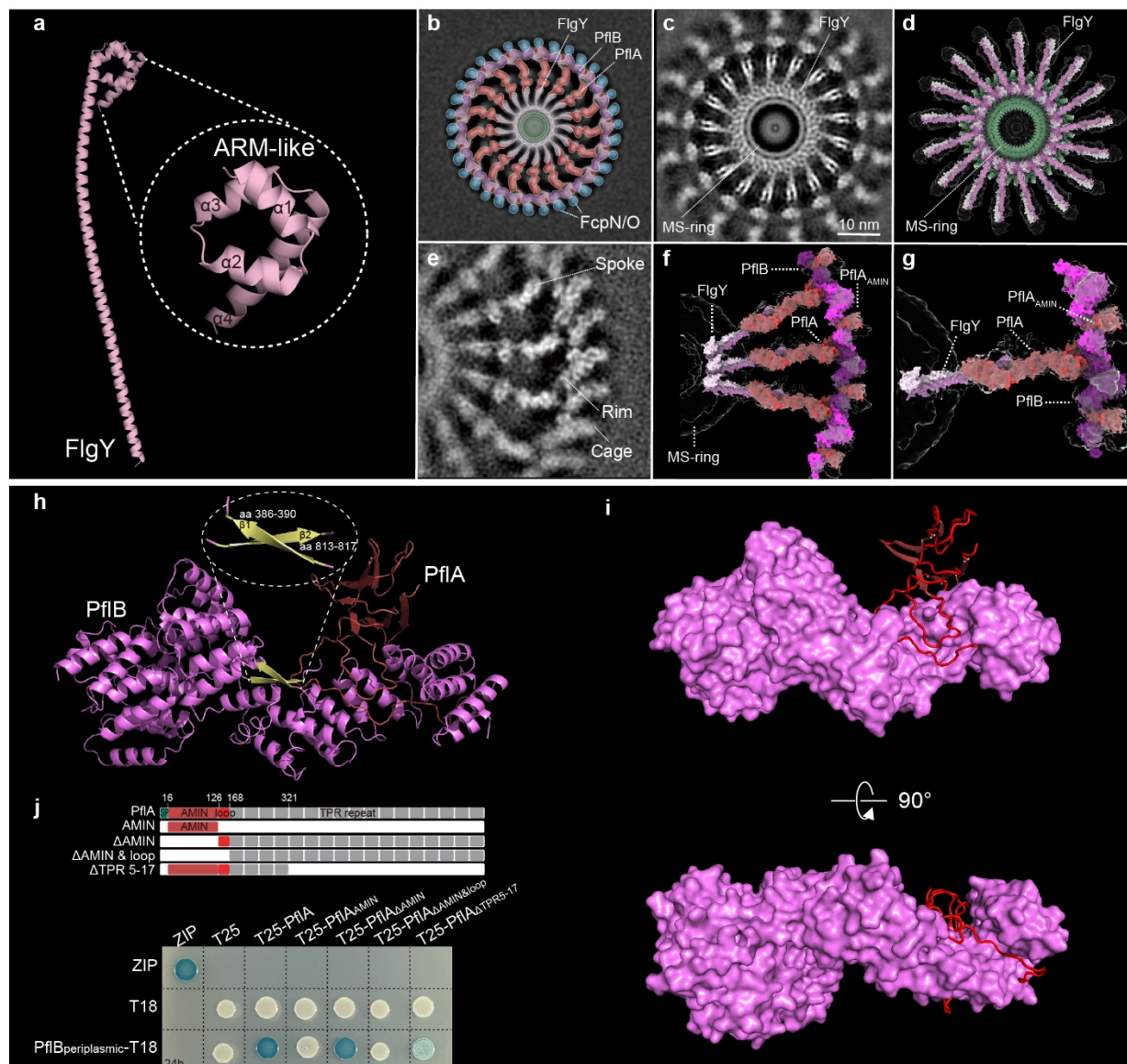
- 1108 71 <https://doi.org/10.1016/j.jsb.2005.07.007>
- 1109 71 Xu, A. & Xu, C. FastTomo: A SerialEM Script for Collecting Electron Tomography Data. *bioRxiv*,  
1110 2021.2003.2016.435675 (2021). <https://doi.org/10.1101/2021.03.16.435675>
- 1111 72 Zheng, S. Q. *et al.* MotionCor2: anisotropic correction of beam-induced motion for improved  
1112 cryo-electron microscopy. *Nature methods* **14**, 331-332 (2017).  
<https://doi.org/10.1038/nmeth.4193>
- 1113 73 Kremer, J. R., Mastronarde, D. N. & McIntosh, J. R. Computer visualization of three-  
1114 dimensional image data using IMOD. *J Struct Biol* **116**, 71-76 (1996).  
<https://doi.org/10.1006/jsbi.1996.0013>
- 1115 74 Mastronarde, D. N. & Held, S. R. Automated tilt series alignment and tomographic  
1116 reconstruction in IMOD. *J Struct Biol* **197**, 102-113 (2017).  
<https://doi.org/10.1016/j.jsb.2016.07.011>
- 1117 75 Zhang, K. Gctf: Real-time CTF determination and correction. *J Struct Biol* **193**, 1-12 (2016).  
<https://doi.org/10.1016/j.jsb.2015.11.003>
- 1118 76 Xiong, Q., Morphew, M. K., Schwartz, C. L., Hoenger, A. H. & Mastronarde, D. N. CTF  
1119 determination and correction for low dose tomographic tilt series. *J Struct Biol* **168**, 378-387  
(2009). <https://doi.org/10.1016/j.jsb.2009.08.016>
- 1120 77 Agulleiro, J. I. & Fernandez, J. J. Tomo3D 2.0--exploitation of advanced vector extensions  
1121 (AVX) for 3D reconstruction. *J Struct Biol* **189**, 147-152 (2015).  
<https://doi.org/10.1016/j.jsb.2014.11.009>
- 1122 78 Morado, D. R., Hu, B. & Liu, J. Using Tomoauto: A Protocol for High-throughput Automated  
1123 Cryo-electron Tomography. *J Vis Exp*, e53608 (2016). <https://doi.org/10.3791/53608>
- 1124 79 Winkler, H. *et al.* Tomographic subvolume alignment and subvolume classification applied to  
1125 myosin V and SIV envelope spikes. *J Struct Biol* **165**, 64-77 (2009).  
<https://doi.org/10.1016/j.jsb.2008.10.004>
- 1126 80 Winkler, H. 3D reconstruction and processing of volumetric data in cryo-electron tomography.  
1127 *J Struct Biol* **157**, 126-137 (2007). <https://doi.org/10.1016/j.jsb.2006.07.014>
- 1128 81 Abramson, J. *et al.* Accurate structure prediction of biomolecular interactions with AlphaFold  
1129 3. *Nature* (2024). <https://doi.org/10.1038/s41586-024-07487-w>
- 1130 82 Guo, S., Xu, H., Chang, Y., Motaleb, M. A. & Liu, J. FliL ring enhances the function of periplasmic  
1131 flagella. *Proceedings of the National Academy of Sciences of the United States of America*  
1132 **119**, e2117245119 (2022). <https://doi.org/10.1073/pnas.2117245119>
- 1133 83 Punjani, A., Rubinstein, J. L., Fleet, D. J. & Brubaker, M. A. cryoSPARC: algorithms for rapid  
1134 unsupervised cryo-EM structure determination. *Nature methods* **14**, 290-296 (2017).  
<https://doi.org/10.1038/nmeth.4169>
- 1135 84 Wang, N. *et al.* Structural basis of human monocarboxylate transporter 1 inhibition by anti-  
1136 cancer drug candidates. *Cell* **184**, 370-383 e313 (2021).  
<https://doi.org/10.1016/j.cell.2020.11.043>
- 1137 85 Xu, K., Wang, Z., Shi, J., Li, H. & Zhang, Q. C. in *Proceedings of the Thirty-Third AAAI  
1138 Conference on Artificial Intelligence and Thirty-First Innovative Applications of Artificial  
1139 Intelligence Conference and Ninth AAAI Symposium on Educational Advances in Artificial  
1140 Intelligence* (2022).
- 1141 85
- 1142 85
- 1143 85
- 1144 85
- 1145 85
- 1146 85
- 1147 85
- 1148 85

- 1149            1149            *Intelligence* Vol. 33 Article 152 (AAAI Press, Honolulu, Hawaii, USA, 2019).
- 1150            86            Emsley, P. & Cowtan, K. Coot: model-building tools for molecular graphics. *Acta Crystallogr D Biol Crystallogr* **60**, 2126-2132 (2004). <https://doi.org/10.1107/S0907444904019158>
- 1151            87            Afonine, P. V. *et al.* Real-space refinement in PHENIX for cryo-EM and crystallography. *Acta Crystallogr D Struct Biol* **74**, 531-544 (2018). <https://doi.org/10.1107/S2059798318006551>
- 1152            88            Battesti, A. & Bouveret, E. The bacterial two-hybrid system based on adenylate cyclase reconstitution in Escherichia coli. *Methods* **58**, 325-334 (2012).  
<https://doi.org/10.1016/j.ymeth.2012.07.018>
- 1153            89            Livak, K. J. & Schmittgen, T. D. Analysis of relative gene expression data using real-time quantitative PCR and the 2(-Delta Delta C(T)) Method. *Methods* **25**, 402-408 (2001).  
<https://doi.org/10.1006/meth.2001.1262>
- 1154            90            Gabler, F. *et al.* Protein Sequence Analysis Using the MPI Bioinformatics Toolkit. *Curr Protoc Bioinformatics* **72**, e108 (2020). <https://doi.org/10.1002/cpb1.108>
- 1155            91            Abby, S. S., Denise, R. & Rocha, E. P. C. Identification of Protein Secretion Systems in Bacterial Genomes Using MacSyFinder Version 2. *Methods Mol Biol* **2715**, 1-25 (2024).  
[https://doi.org/10.1007/978-1-0716-3445-5\\_1](https://doi.org/10.1007/978-1-0716-3445-5_1)
- 1156            92            Letunic, I., Khedkar, S. & Bork, P. SMART: recent updates, new developments and status in 2020. *Nucleic acids research* **49**, D458-D460 (2021). <https://doi.org/10.1093/nar/gkaa937>
- 1157            93            Denise, R., Abby, S. S. & Rocha, E. P. C. Diversification of the type IV filament superfamily into machines for adhesion, protein secretion, DNA uptake, and motility. *PLoS Biol* **17**, e3000390 (2019). <https://doi.org/10.1371/journal.pbio.3000390>
- 1158            94            Na, S. I. *et al.* UBCG: Up-to-date bacterial core gene set and pipeline for phylogenomic tree reconstruction. *J Microbiol*, 5 (2018). <https://doi.org/10.1007/s12275-018-8014-6>
- 1159            95            Galperin, M. Y. *et al.* COG database update 2024. *Nucleic acids research* **53**, D356-D363 (2025).  
<https://doi.org/10.1093/nar/gkae983>
- 1160            96            Parks, D. H., Imelfort, M., Skennerton, C. T., Hugenholtz, P. & Tyson, G. W. CheckM: assessing the quality of microbial genomes recovered from isolates, single cells, and metagenomes. *Genome research* **25**, 1043-1055 (2015). <https://doi.org/10.1101/gr.186072.114>
- 1161            97            Camacho, C. *et al.* BLAST+: architecture and applications. *BMC Bioinformatics* **10**, 421 (2009).  
<https://doi.org/10.1186/1471-2105-10-421>
- 1162            98            Chaumeil, P. A., Mussig, A. J., Hugenholtz, P. & Parks, D. H. GTDB-Tk v2: memory friendly classification with the genome taxonomy database. *Bioinformatics* **38**, 5315-5316 (2022).  
<https://doi.org/10.1093/bioinformatics/btac672>
- 1163            99            Nguyen, L. T., Schmidt, H. A., von Haeseler, A. & Minh, B. Q. IQ-TREE: a fast and effective stochastic algorithm for estimating maximum-likelihood phylogenies. *Mol Biol Evol* **32**, 268-274 (2015). <https://doi.org/10.1093/molbev/msu300>
- 1164            100            Letunic, I. & Bork, P. Interactive Tree of Life (iTOL) v6: recent updates to the phylogenetic tree display and annotation tool. *Nucleic acids research* **52**, W78-W82 (2024).  
<https://doi.org/10.1093/nar/gkae268>
- 1165            101            Johnson, L. S., Eddy, S. R. & Portugaly, E. Hidden Markov model speed heuristic and iterative HMM search procedure. *BMC Bioinformatics* **11**, 431 (2010). <https://doi.org/10.1186/1471-412X-11-431>

- 1190                   2105-11-431
- 1191   102 Karpenahalli, M. R., Lupas, A. N. & Soding, J. TPRpred: a tool for prediction of TPR-, PPR- and  
1192                   SEL1-like repeats from protein sequences. *BMC Bioinformatics* **8**, 2 (2007).  
<https://doi.org/10.1186/1471-2105-8-2>
- 1193   103 D'Andrea, L. D. & Regan, L. TPR proteins: the versatile helix. *Trends Biochem Sci* **28**, 655-662  
1195                   (2003). <https://doi.org/10.1016/j.tibs.2003.10.007>
- 1196   104 Teufel, F. *et al.* SignalP 6.0 predicts all five types of signal peptides using protein language  
1197                   models. *Nature biotechnology* **40**, 1023-1025 (2022). <https://doi.org/10.1038/s41587-021-01156-3>
- 1199   105 Moller, S., Croning, M. D. & Apweiler, R. Evaluation of methods for the prediction of  
1200                   membrane spanning regions. *Bioinformatics* **17**, 646-653 (2001).  
<https://doi.org/10.1093/bioinformatics/17.7.646>
- 1202



**Fig. 1. Mapping components in *C. jejuni* motor.** **a**, Cut-through view of the organization of the *C. jejuni* motor in situ, with a focus on periplasmic scaffolds below the medial disk. Color scheme for proteins or complexes is indicated below and the E-ring in both light and dark pink represents dimer of FlgY. **b-i**, Each column with four images from top to bottom contains central section of motor structure, cross-section of stator region, cross-section of proximal disk region (refined), and cartoon representation of proximal disk region, from wild type or seven flagellar gene mutants. Scale bar in **b**, 20 nm, applies to columns **b** through **i**. Color scheme in cartoon representations follows the same as in **a**.



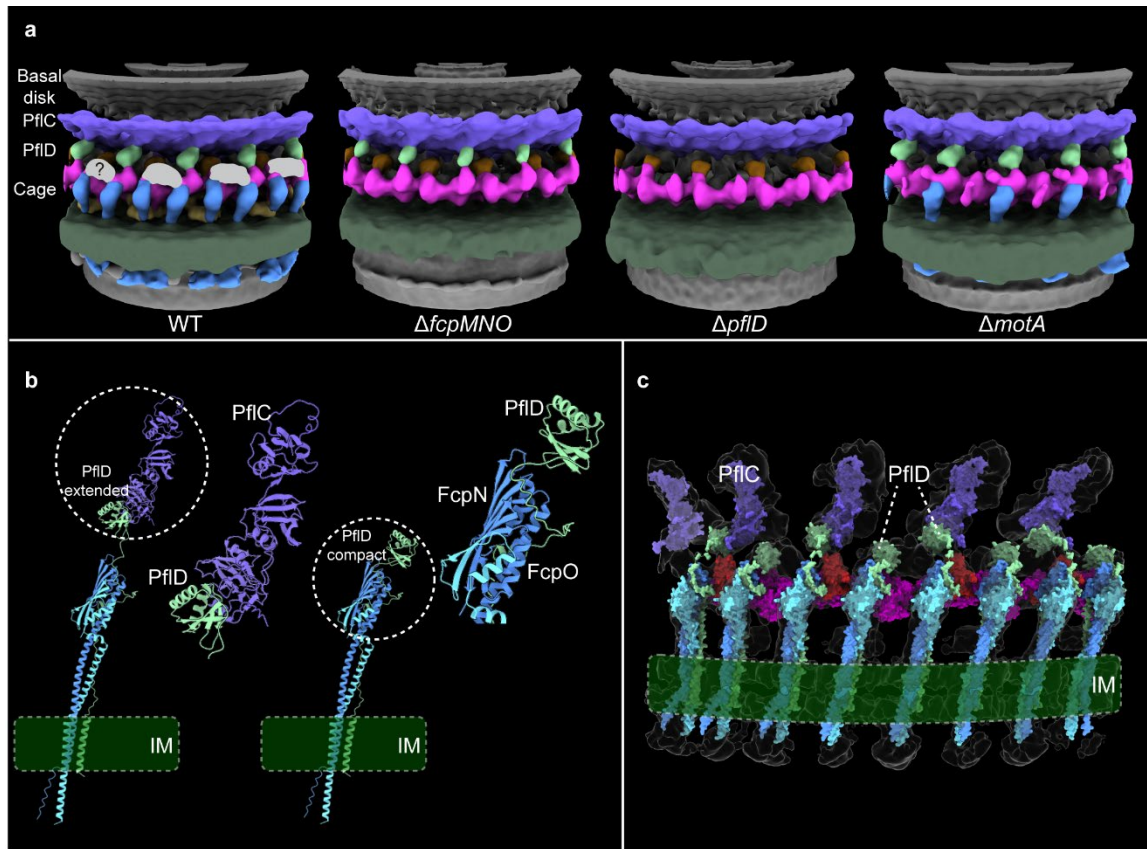


**Fig. 3. PflD in two conformations form different tetrameric cage units with FcpMNO.** **a**, Comparison of 3D views of motor structures (isosurface rendering) from wild type and three mutants  $\Delta fcpMNO$ ,  $\Delta pflD$ , and  $\Delta motA$ . Below the medial disk (purple), PflD is highlighted in green, PflB rim in magenta, and cage units in blue. The unknown density between two cage units next to PflD position is in grey and marked with question mark (?). **b**, AlphaFold-Multimer predicted structures of the PflD (light green)-FcpNO (dark and light blue) complex with two conformations. Left: PflD with extended PflD<sub>PilP-loop</sub> connecting PflC spoke (purple) by PflD<sub>PilQ-N1</sub> domain; right: PflD with contracted PflD<sub>PilP-loop</sub> making its PflD<sub>PilQ-N1</sub> domain closer to FcpNO and detaching from PflC spoke. **c**, PflD-FcpNO complexes in two conformations fitted into the segmented cryo-ET map (transparent).

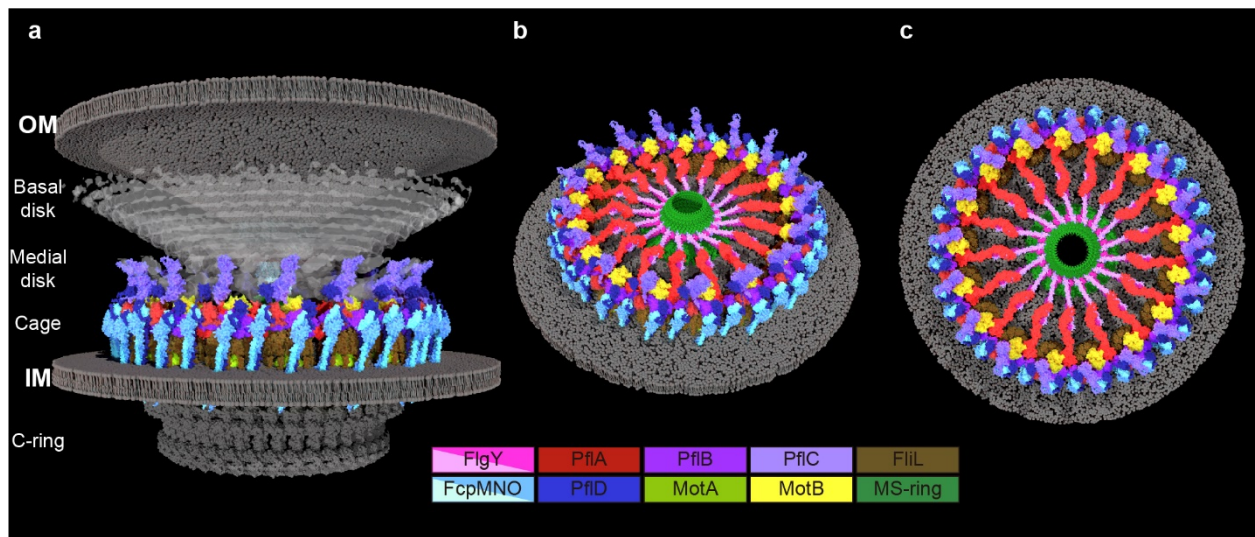


**Fig. 4. Model of *C. jejuni* flagellar motor.** **a**, Cut-through view of *C. jejuni* motor built by docking structures of components listed below. Color scheme is also indicated below and structure source for proteins or complexes are indicated in Materials and Method. **b-c**, Tilted and top view of *C. jejuni* motor, removing top part to reveal the inner-membrane proximal scaffold components.

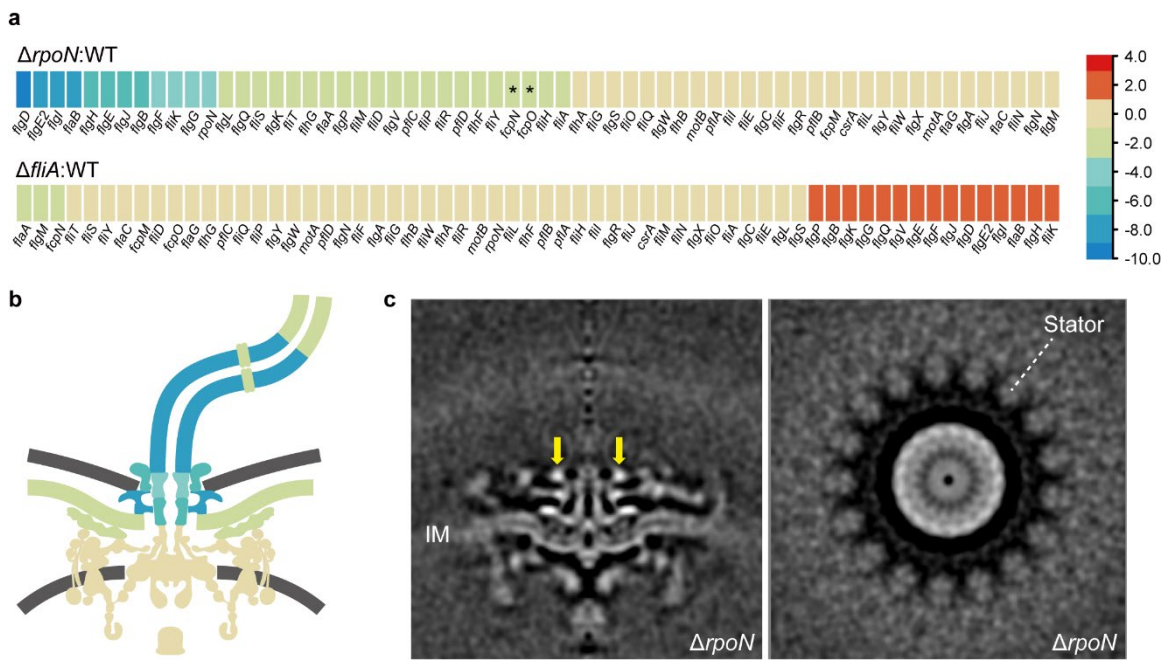


**Fig. 5. The assembly order of *C. jejuni* motor.** **a**, Relative expression level of flagellar genes in two *C. jejuni* mutants  $\Delta rpoN$  and  $\Delta fliA$  compared to wild type, revealed by RNA-seq. The colors in the heatmaps are defined by  $\log_2(\text{fold change})$  of FPKM values of mutant compared to wild type as indicated on the right and Methods. Asterisks (\*) denote that the expression levels of *fcpN* and *fcpO* are very low in all nine samples of RNA-seq. **b**, Cartoon of motor structure from wild-type *C. jejuni* with components colored by  $\log_2(\text{fold change})$  values of  $\Delta rpoN$  mutant compared to wild type as indicated in **a**. **c**, Central section (left) and cross-section (right) of motor structure from  $\Delta rpoN$  mutant revealed the early assembly of inner-membrane proximal scaffolds and stator complexes before the rod. A transient periplasmic ring above the E-ring is highlighted by yellow arrow.

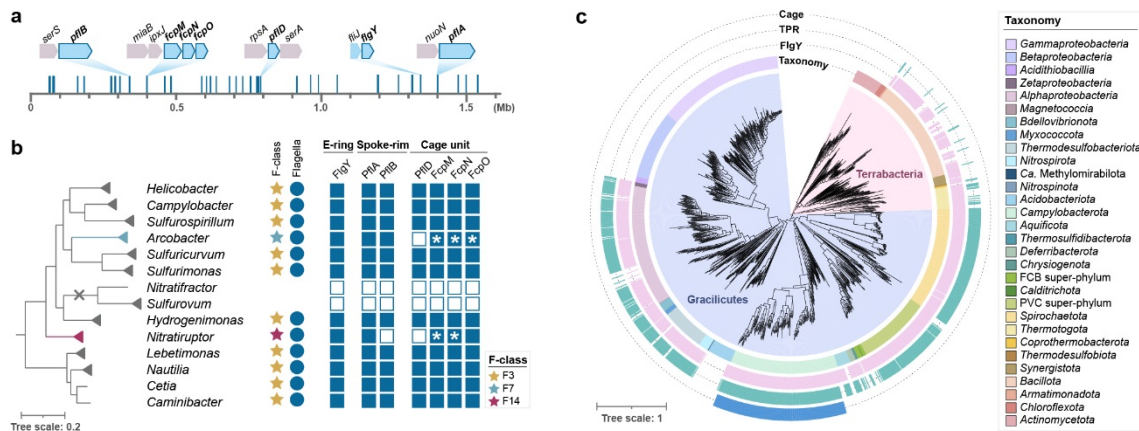
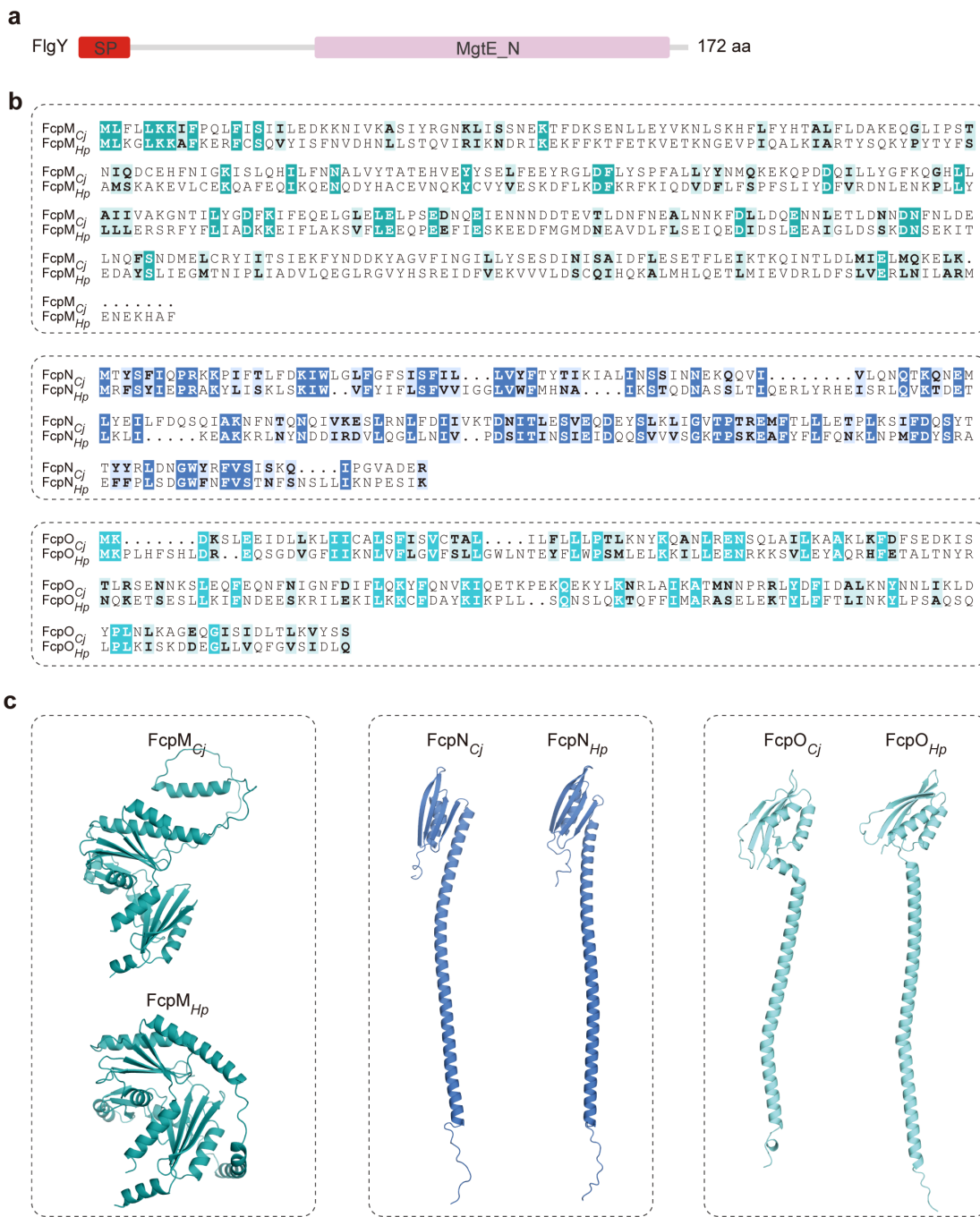
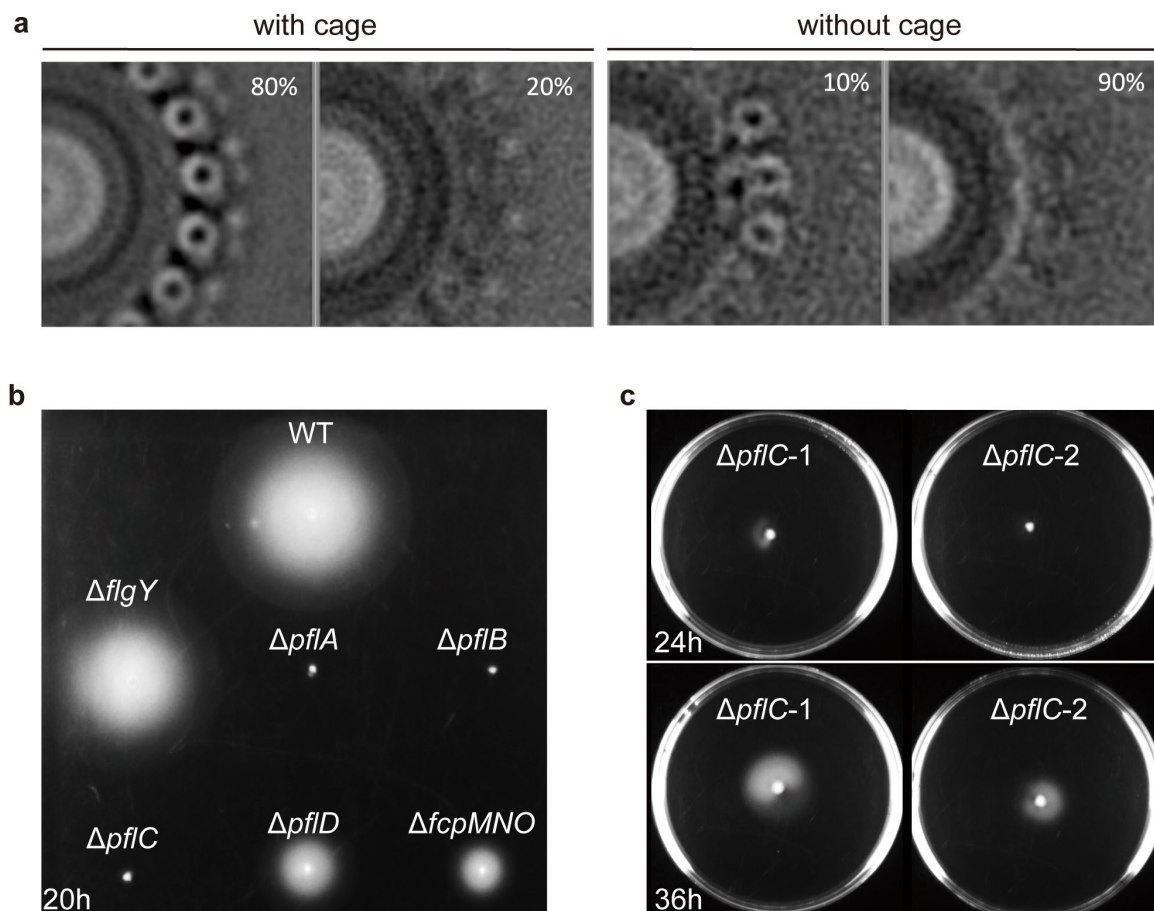


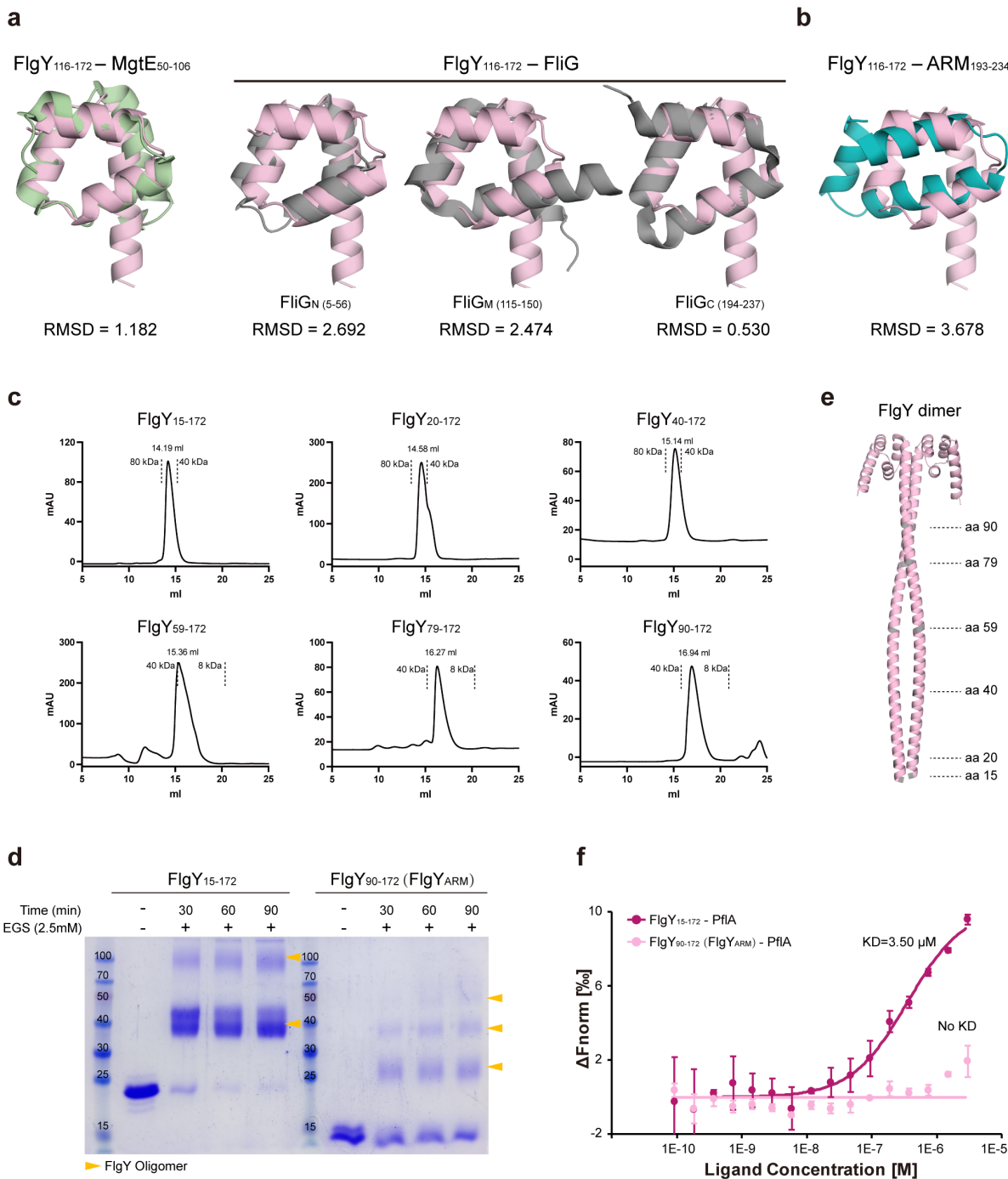
**Fig. 6 Evolution of inner-membrane proximal scaffolding proteins.** **a**, The distribution of flagellar genes (represented by blue lines) in linearized genome of *C. jejuni* 81-176 and the conserved gene order of *flgY*, *pflA*, *pflB*, *pflD*, *fcpMNO* in the phylum *Campylobacterota*. Details of gene order for each species of *Campylobacterota* is provided in Extended Data Fig. 8-9. **b**, The co-occurrence of inner-membrane proximal scaffolds and the F3 chemosensory class in *Campylobacterota*. Left: the phylogenetic tree of *Campylobacterota* taken from (ref. 30), with *Wolinella* genus grouped into its close relative *Helicobacter* clade and two branches highlighted for *Arcobacter* (blue) and *Nitratiruptor* (red) that have non-F3 chemosensory class; Middle: the chemosensory F class controlling flagellar motility and the presence of flagellar gene sets across genera; Right: the presence (solid squares) and absence (hollow squares) of components of inner-membrane proximal scaffolds. Asterisks (\*) denote fusion of genes *fcpMNO* or *fcpMN* in *Arcobacter* and *Nitratiruptor*, respectively. **c**, Phylogenetic distribution of proteins constituting E-ring, spokes, and cage in the *Bacteria* domain. The maximum likelihood tree of 1,365 flagellated species based on concatenated 120 marker proteins is rooted between *Terrabacteria* (peach) and *Gracilicutes* (lavender). The innermost ring is color-coded to represent the taxonomy of each species with the taxon listed on the right, while the outer rings feature colored blocks to indicate the presence of FlgY, TPR repeat proteins in proximity to flagellar gene cluster, and cage proteins.



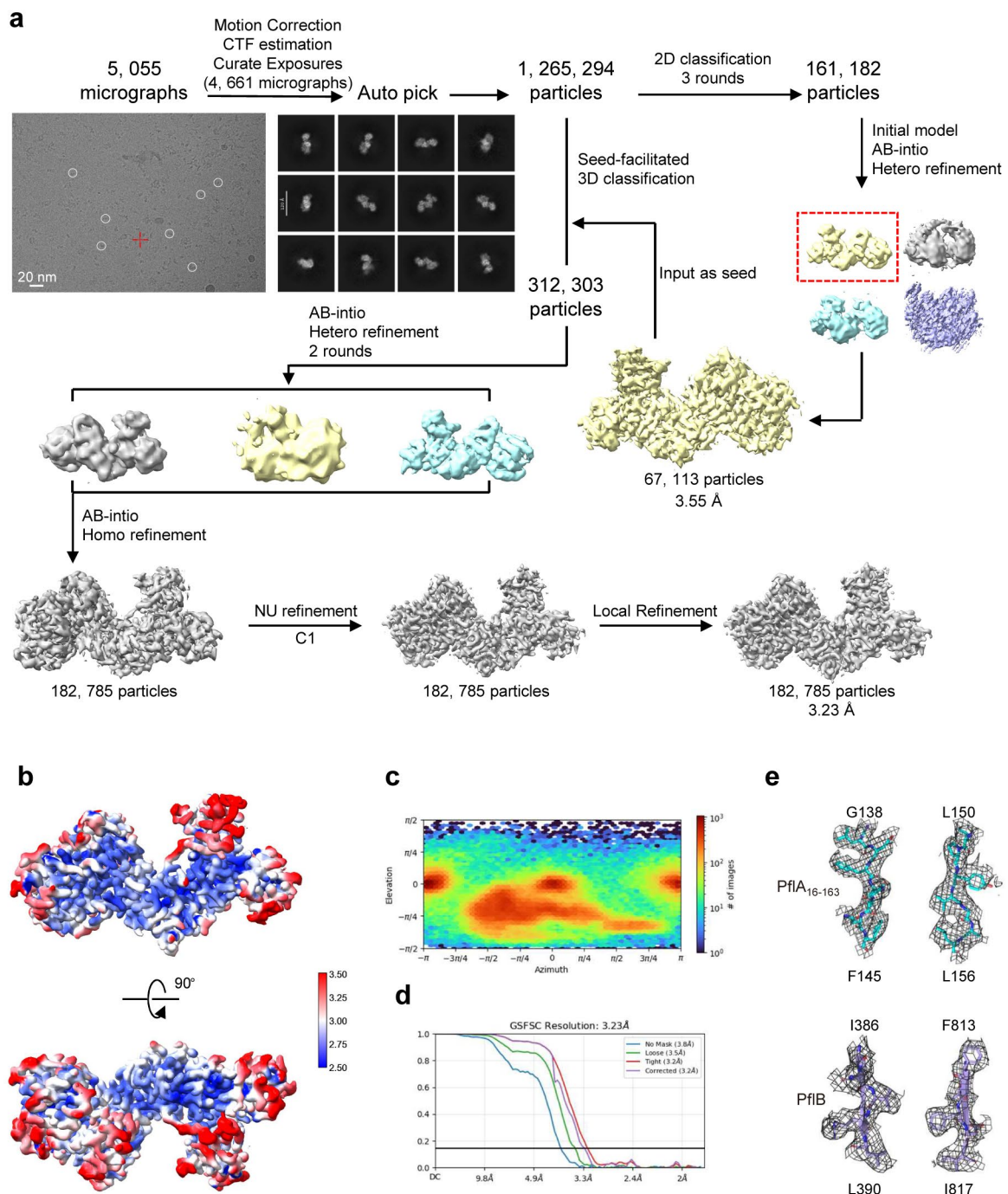
**Extended Data Figure 1. Sequence and structural analyses of FlgY and FcpMNO.** **a**, SMART motif analysis of FlgY (WP\_002855458.1) suggested a single peptide (SP) at its N-terminus and a MgtE\_N domain at C-terminus. **b**, Sequence alignment of FcpM (WP\_002868795.1), FcpN (WP\_002868796.1), and FcpO (WP\_002859017.1) to their homologs in *H. pylori* (WP\_000911905.1, WP\_001212813.1, WP\_001212813.1). **c**, Comparison of AlphaFold3-predicted structures of FcpM, FcpN, and FcpO from *C. jejuni* and *H. pylori*. Sequences for structural prediction are the same as in **b**.



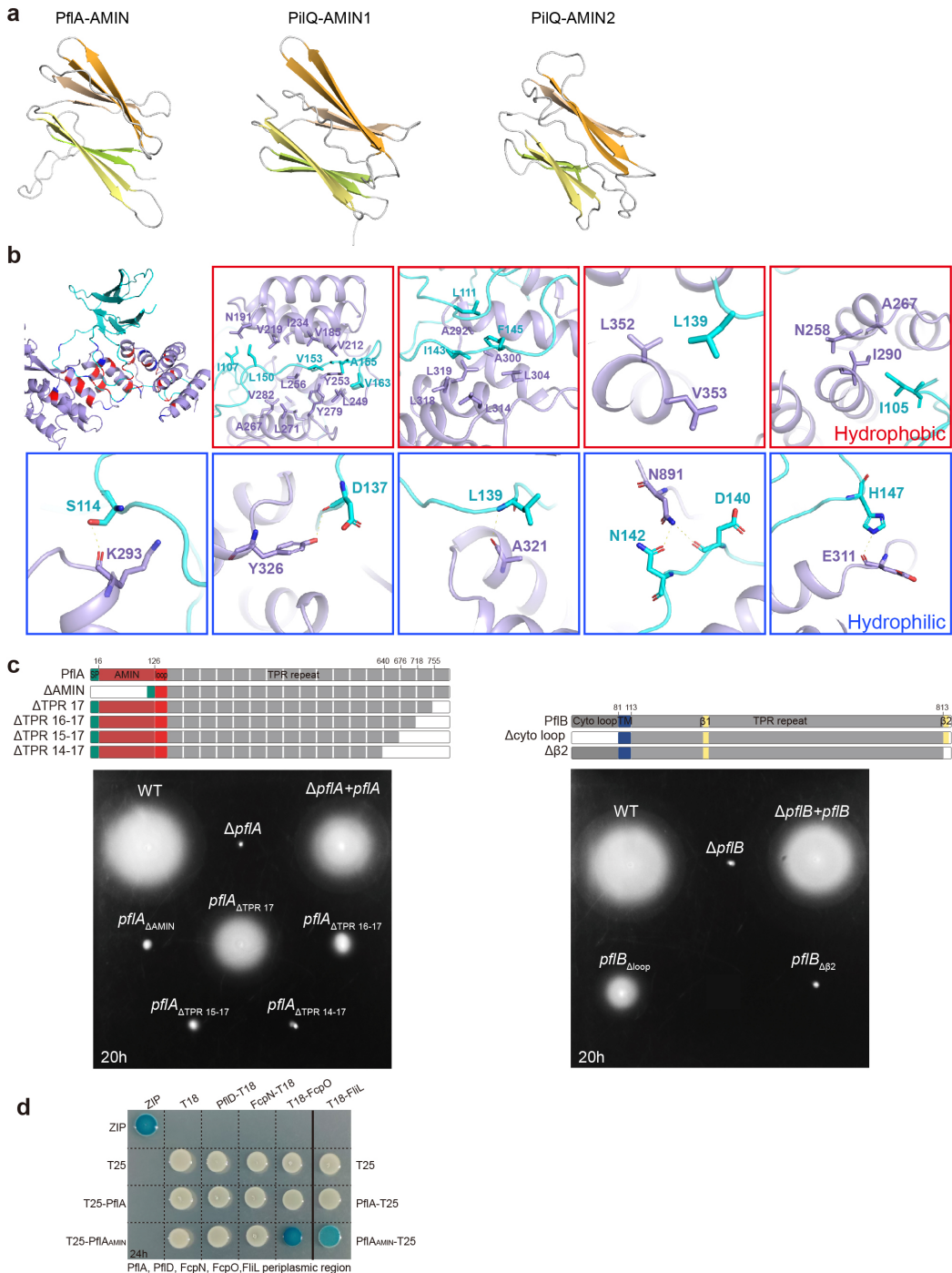
**Extended Data Figure 2. Stator occupancy and motility of WT *C. jejuni* and mutants. a**, Cross-section of motor structure in stator ring region from WT and  $\Delta fcpMNO$  mutant to compare stator occupancy with cage (WT) and without cage ( $\Delta fcpMNO$  mutant). **b**, Soft agar motility assay of WT and six mutants imaged at 20 h. **c**, Soft agar motility assay of  $\Delta pflC$  mutant imaged at 24 h and 36 h, showing reduced but not abolished motility.



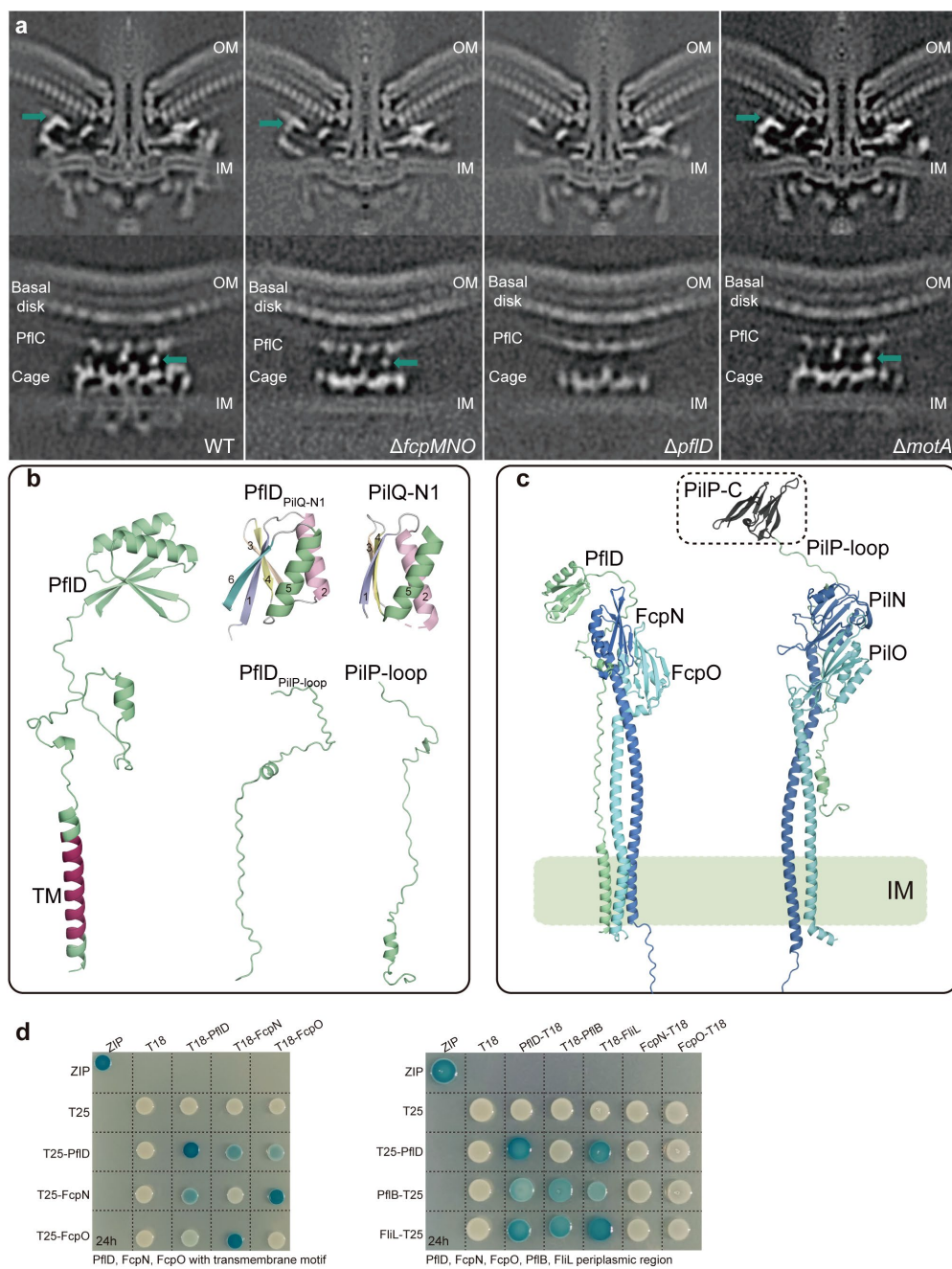
**Extended Data Figure 3. Structural analyses of FlgY.** **a**, Structural overlap of FlgY C-terminal globular domain (predicted by AlphaFold3) with MgtE\_N domain of MgtE (PDB: 2YVX) or three ARM-like domains of FliG (PDB: 3HJL). **b**, Structural overlap of FlgY C-terminal globular domain with canonical ARM repeat of  $\beta$ -catenin (PDB: 3BCT). **c**, Size-exclusion chromatography (SEC) profile of purified FlgY<sub>15-172</sub> and different truncation variants. **d**, Crosslinking of purified FlgY<sub>15-172</sub> and FlgY<sub>90-172</sub> by adding Ethylene glycol bis(succinimidyl succinate) (EGS). Since FlgY<sub>90-172</sub> is mainly composed of the ARM-like domain and forms a dimer that fits the cryo-ET map of the E-ring, we use FlgY<sub>90-172</sub> to represent the dimeric FlgY<sub>ARM</sub>. **e**, AlphaFold3-predicted structure of FlgY dimer. **f**, MST assays of FlgY or FlgY<sub>ARM</sub> with PflA to detect their interaction.



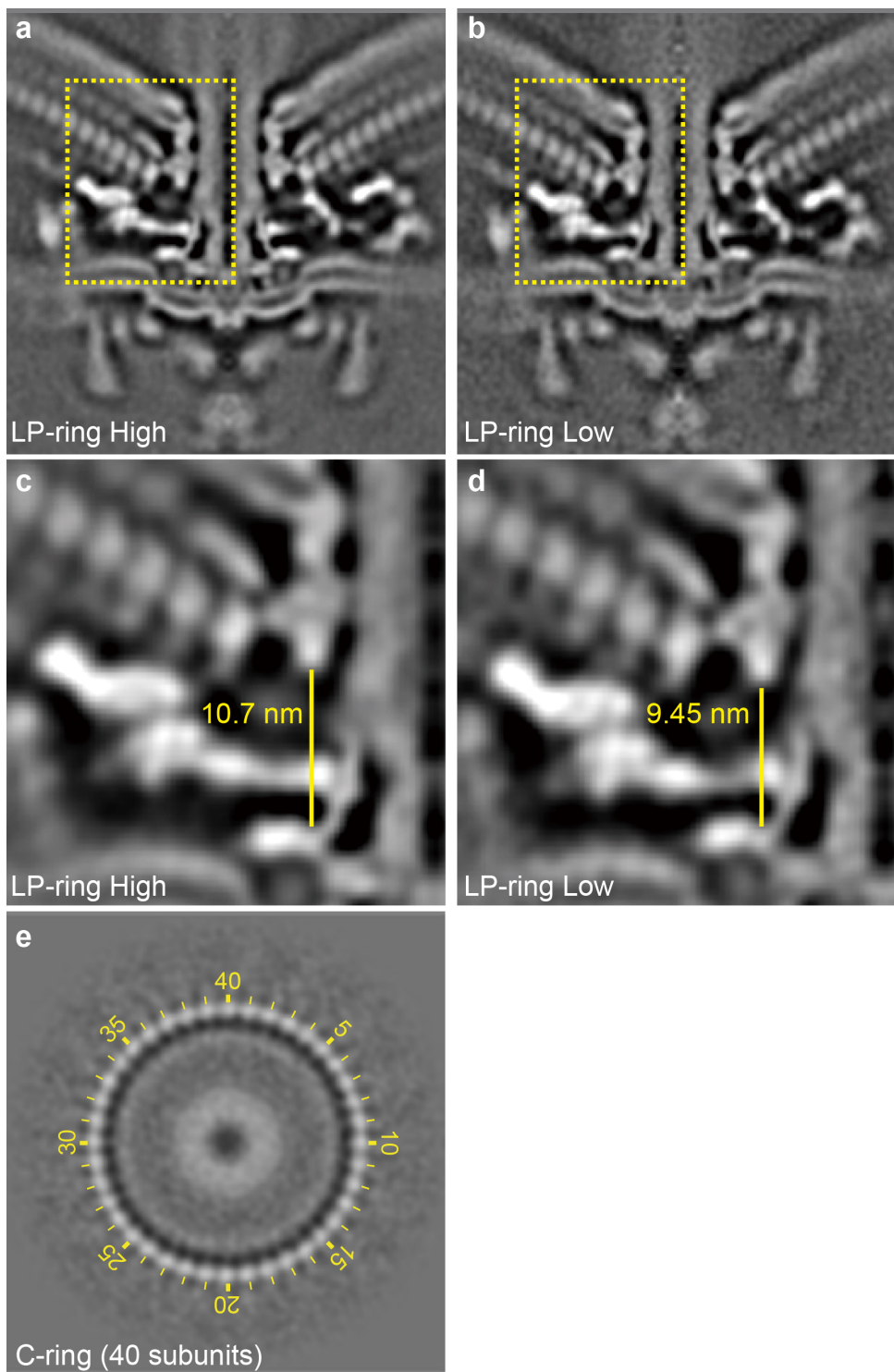
**Extended Data Figure 4. Cryo-EM structural determination of PflA<sub>16-163</sub>-PflB complex.** **a.** Flowchart for cryo-EM data processing of the PflA<sub>16-163</sub>-PflB<sub>178-820</sub> complex. Details can be found in Methods. The complex with C1 symmetry was reconstructed at 3.23 Å resolution. **b.** Local resolution estimations for the EM density map of the PflA<sub>16-163</sub>-PflB<sub>178-820</sub> complex. **c.** Angular distribution of the particles used for reconstruction of the PflA<sub>16-163</sub>-PflB<sub>178-820</sub> complex. **d.** Gold standard Fourier Shell Correlation (FSC) curves of the PflA<sub>16-163</sub>-PflB<sub>178-820</sub> complex. **e.** Representative Cryo-EM densities in the PflA<sub>16-163</sub>-PflB<sub>178-820</sub> complex. The maps, shown as grey mesh, are contoured at 5–6σ.



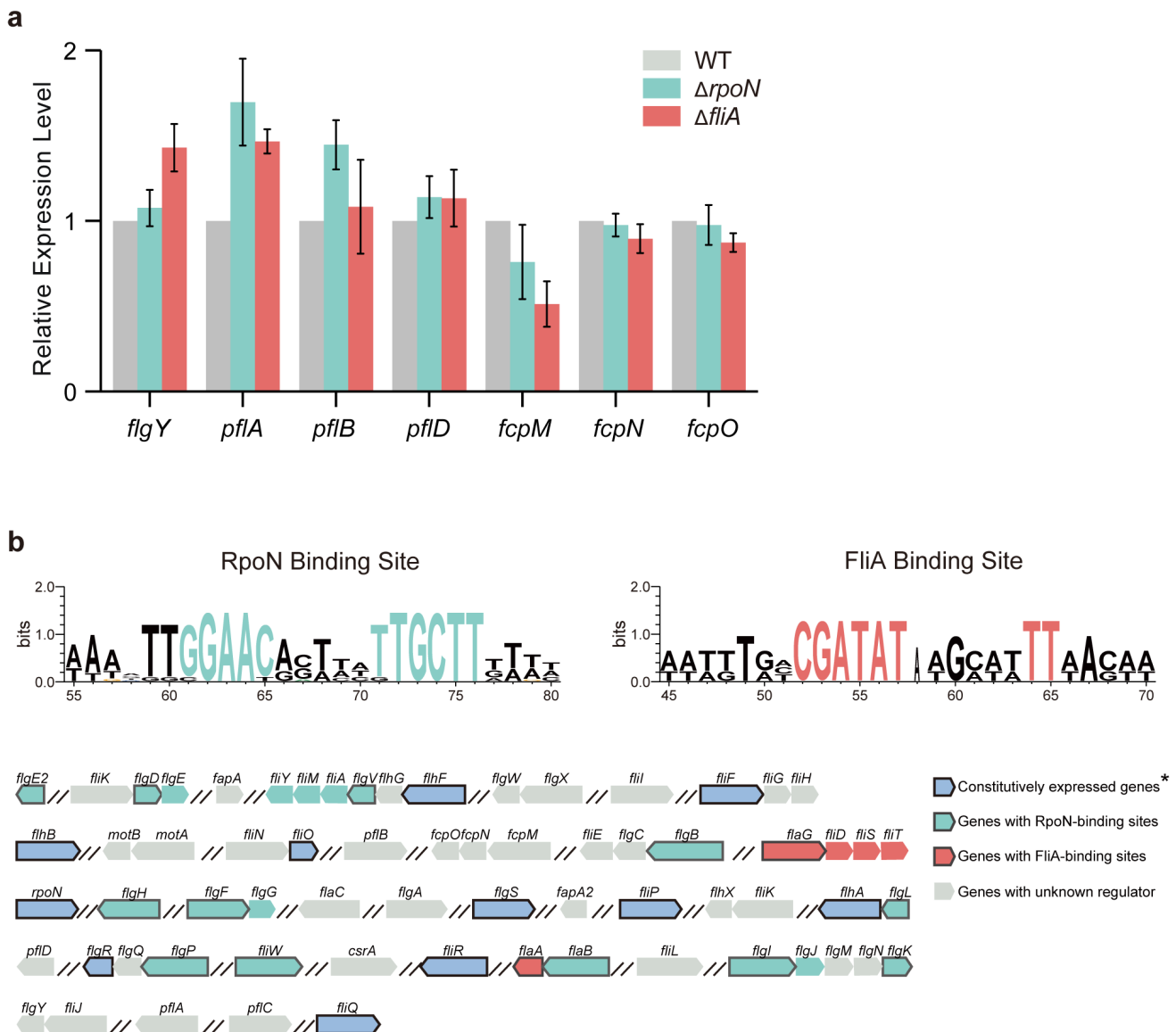
**Extended Data Figure 5. Structural analyses of PflA and PflB.** **a**, Structural comparison of the β-sandwich domain of PflA with AMIN1 and AMIN2 domains of PilQ (PDB:3JC8) of T4P. **b**, Structural details of PflAB interaction interface for both hydrophobic and hydrophilic interactions. **c**, Soft agar motility assay of complementation of various truncations of PflA or PflB into  $\Delta pflA$  or  $\Delta pflB$  mutant, respectively. The domain organization of full-length PflA or PflB and their various truncation constructs made for soft agar motility analyses were indicated on the top. **d**, BTH analysis for the interaction of PflA or PflA<sub>AMIN</sub> domain with PflD, FcpN, FcpO, and Fll. All these proteins were cloned with their periplasmic region only.



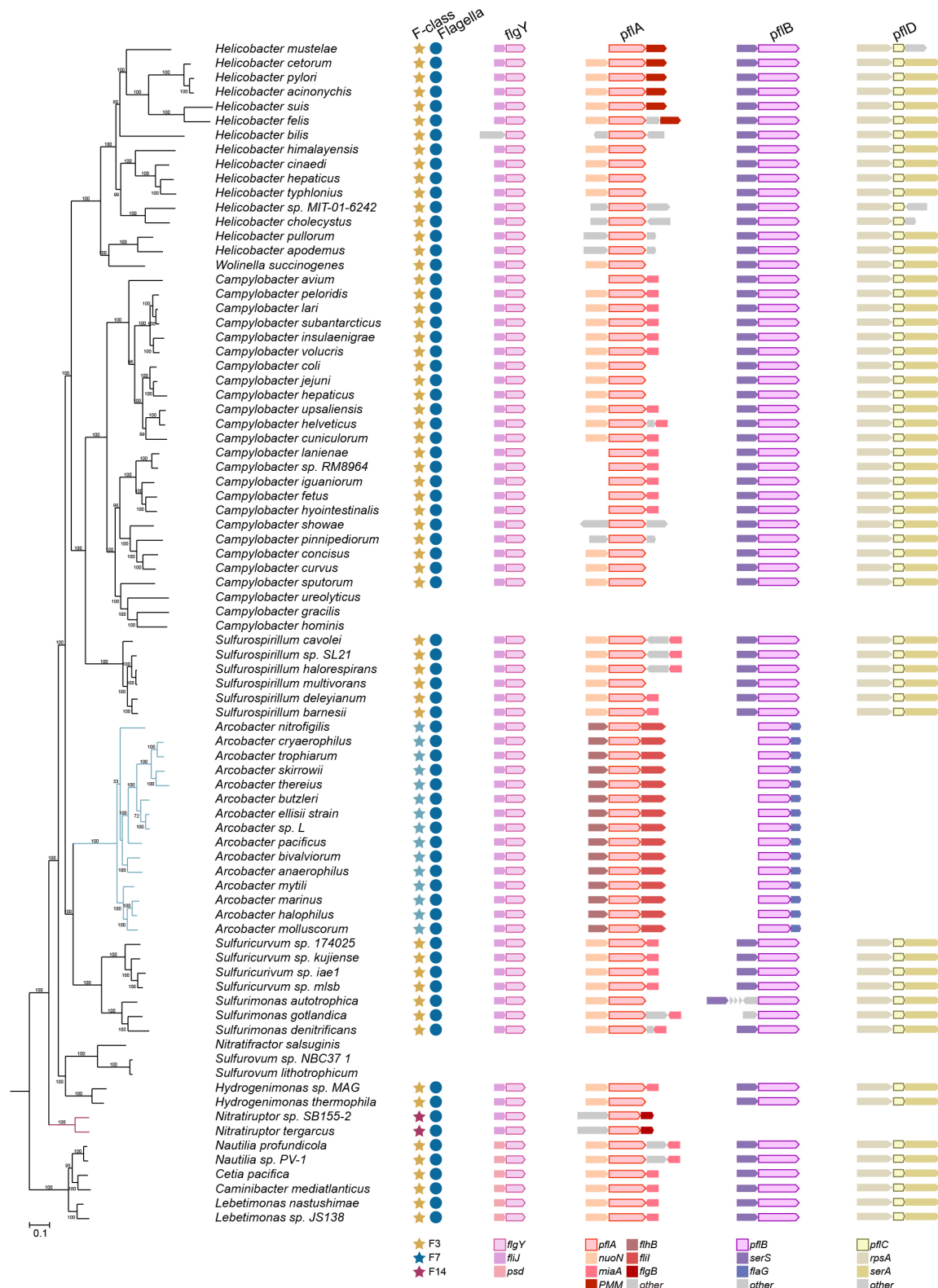
**Extended Data Figure 6. The location of PflD in motor and its interaction with FcpNO.** **a**, The central cross section of the complete motor structure (top) and side view of the cage region (bottom) from WT and three mutants. The position of PflD is indicated with a green arrow. **b**, Left: AlphaFold3-predicted structure of PflD with transmembrane motif highlighted in red. Right: The C-terminal domain and middle loop region of PflD show structural similarity to the N1 domain of PilQ and the loop region of PilP, respectively. **c**, Comparison of complex structure of PflD-FcpNO predicted by AlphaFold-Multimer and PilNOP of T4P (PDB:3JC8). **d**, BTH analysis for the interaction of PflD and FcpNO or other proteins. Left: the interaction of PflD and FcpNO with their transmembrane motif and the T25 or T18 tags were cloned at the N-terminal end next to transmembrane motif; Right: the interaction of PflD and other proteins with periplasmic region only.



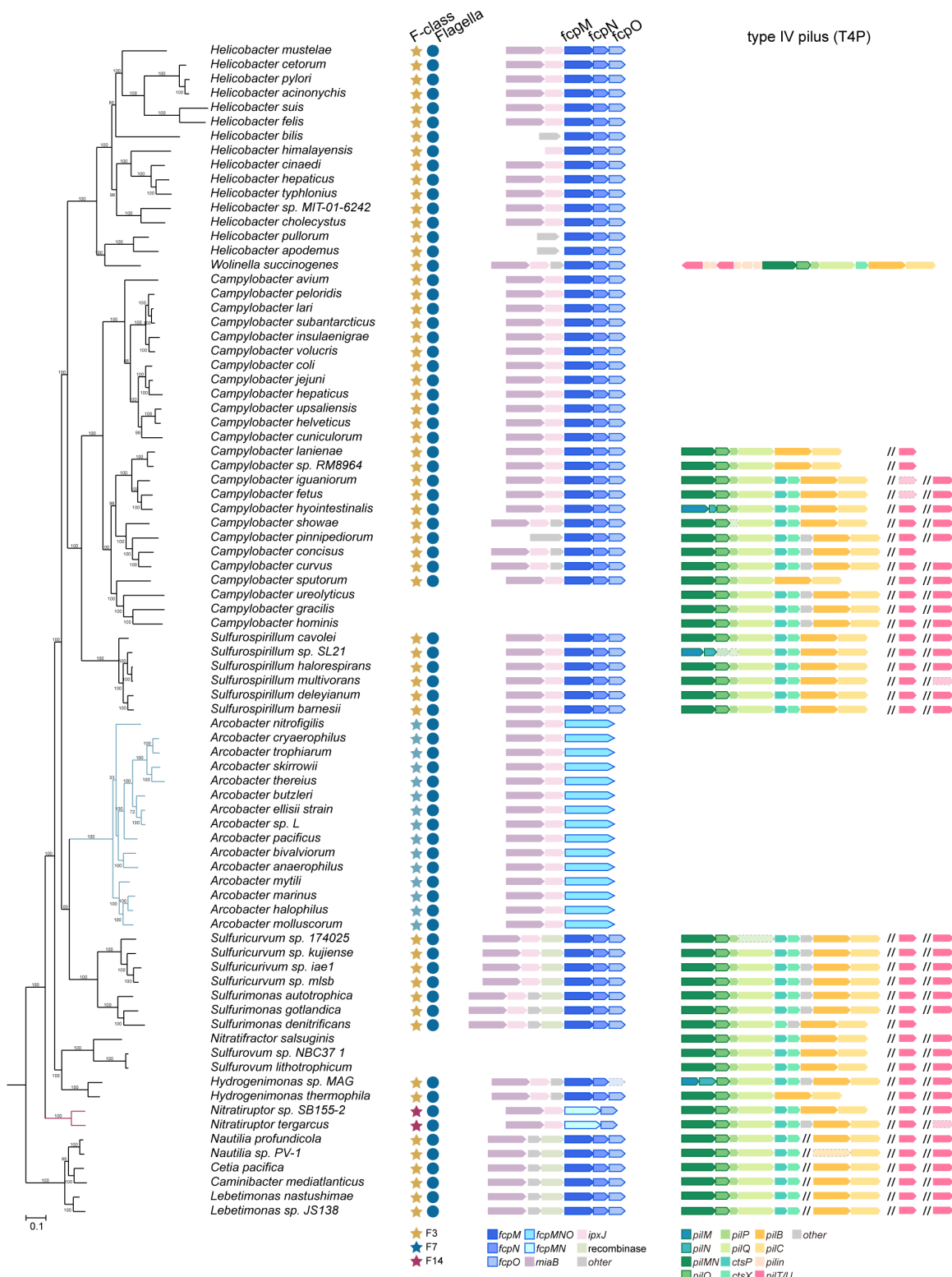
**Extended Data Figure 7. Dynamic changes and C-ring symmetry of *C. jejuni* motor.** **a-b**, Central section of motor structures from WT *C. jejuni* with two distinctive heights from LP-ring to MS-ring. **c-d**, Close-up views of boxed regions in **a** and **b** with measured height from LP-ring to MS-ring, respectively. **e**, Focused classification on the C-ring reveals its 40 subunits.



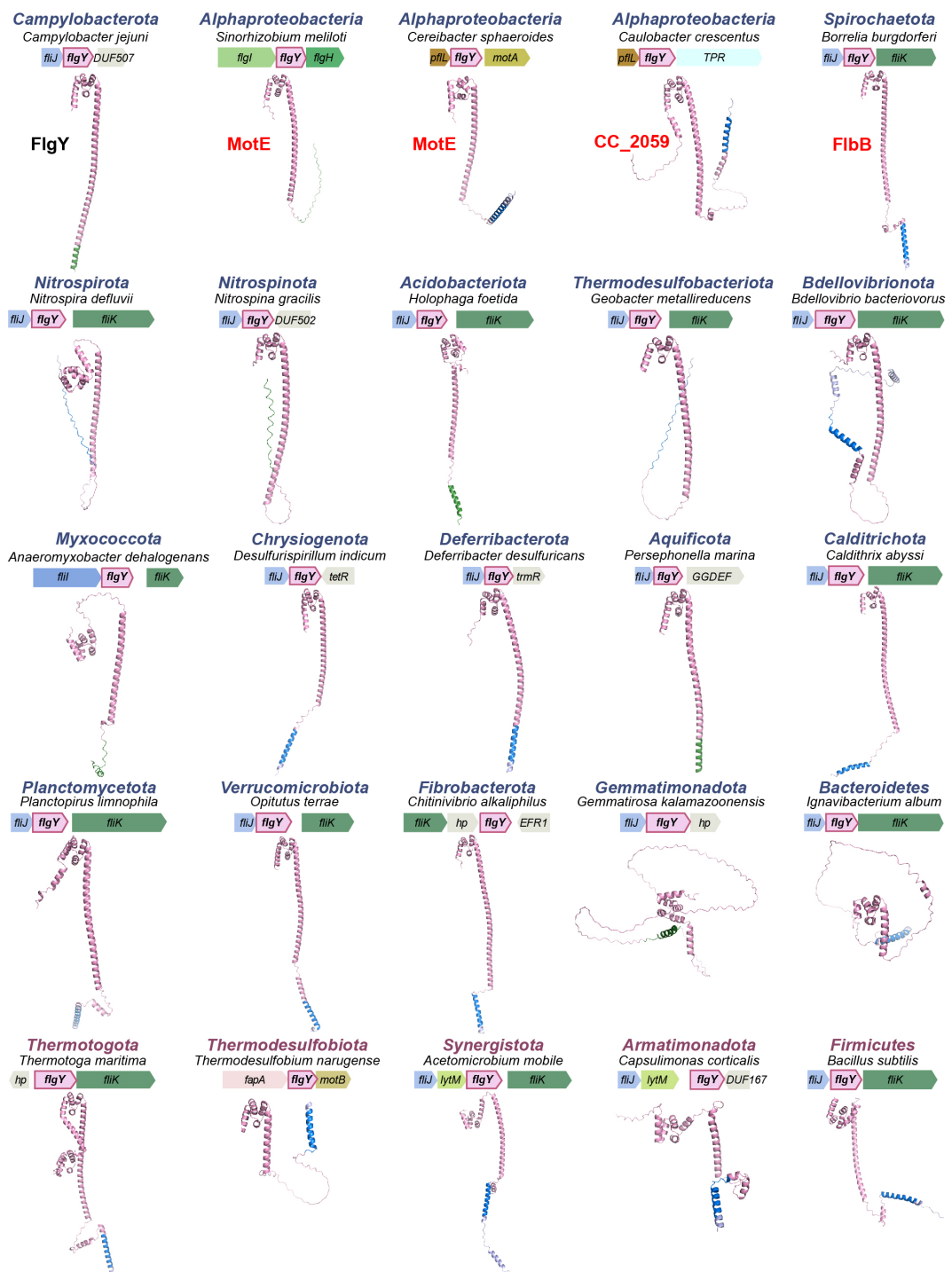
**Extended Data Figure 8. The regulation of *flgY*, *pflA*, *pflB*, *pflD*, and *fcpMNO*.** **a**, qPCR analyses of expression level of seven genes from  $\Delta rpoN$  or  $\Delta fliA$  mutant compared to WT. Data are presented as mean from three independent experiments. No statistically significant differences were observed compared to the wild-type control at the threshold of p-value  $< 0.001$ . **b**, Promoter region analyses of flagellar genes/operons in *C. jejuni* 81-176 to show the presence or absence of RpoN- or FliA- binding sites. The RpoN- or FliA- binding motif shown on the top are taken from reference <sup>1</sup>. Constitutively expressed genes marked with an asterisk are information adopted from reference <sup>2,3</sup>.



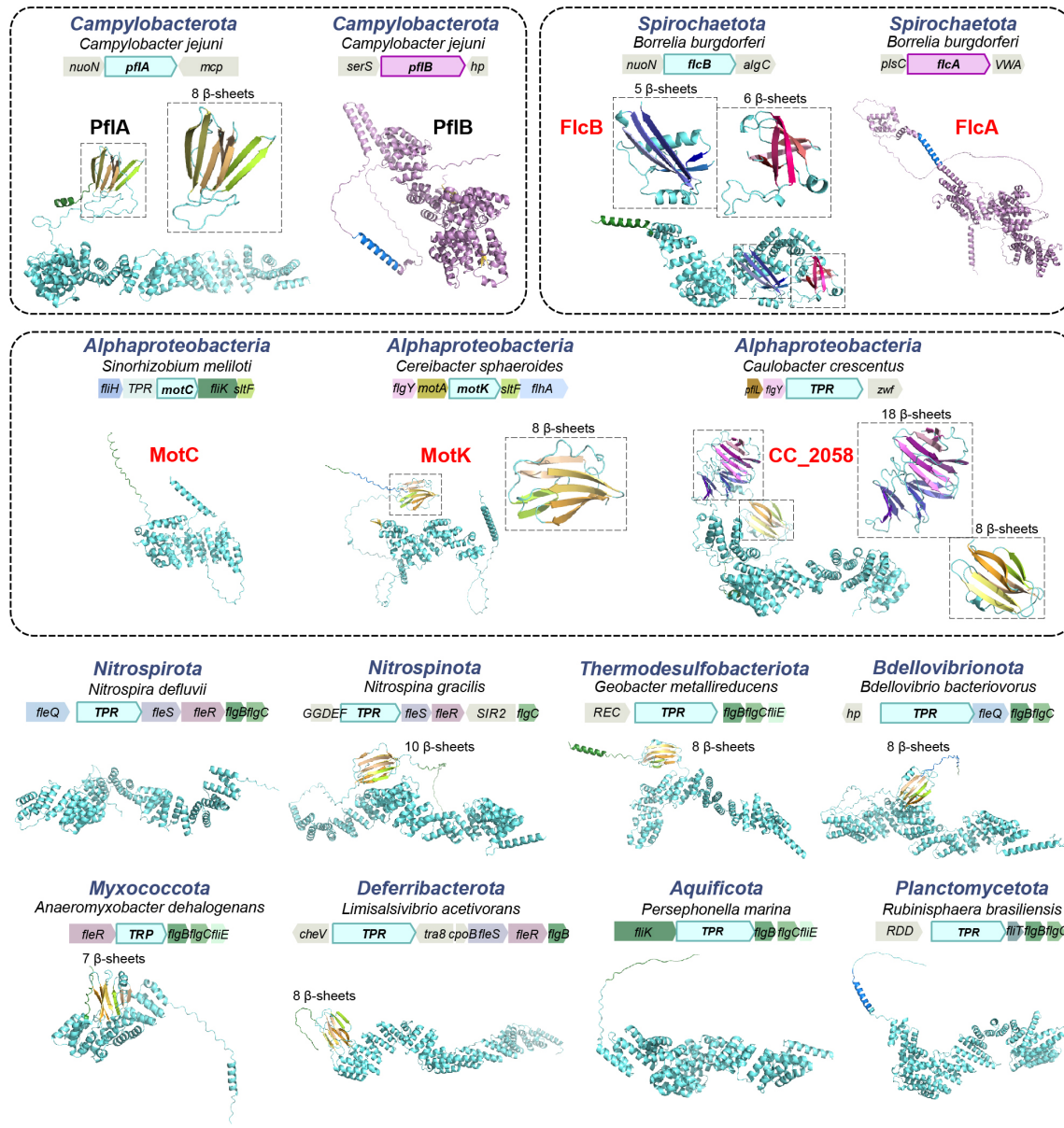
**Extended Data Figure 9. The conserved gene order of *flgY*, *pflA*, *pflB*, and *pflD* in *Campylobacterota* genomes.** Branches were highlighted for *Arcobacter* (blue) and *Nitratiruptor* (red) that have non-F3 chemosensory class.



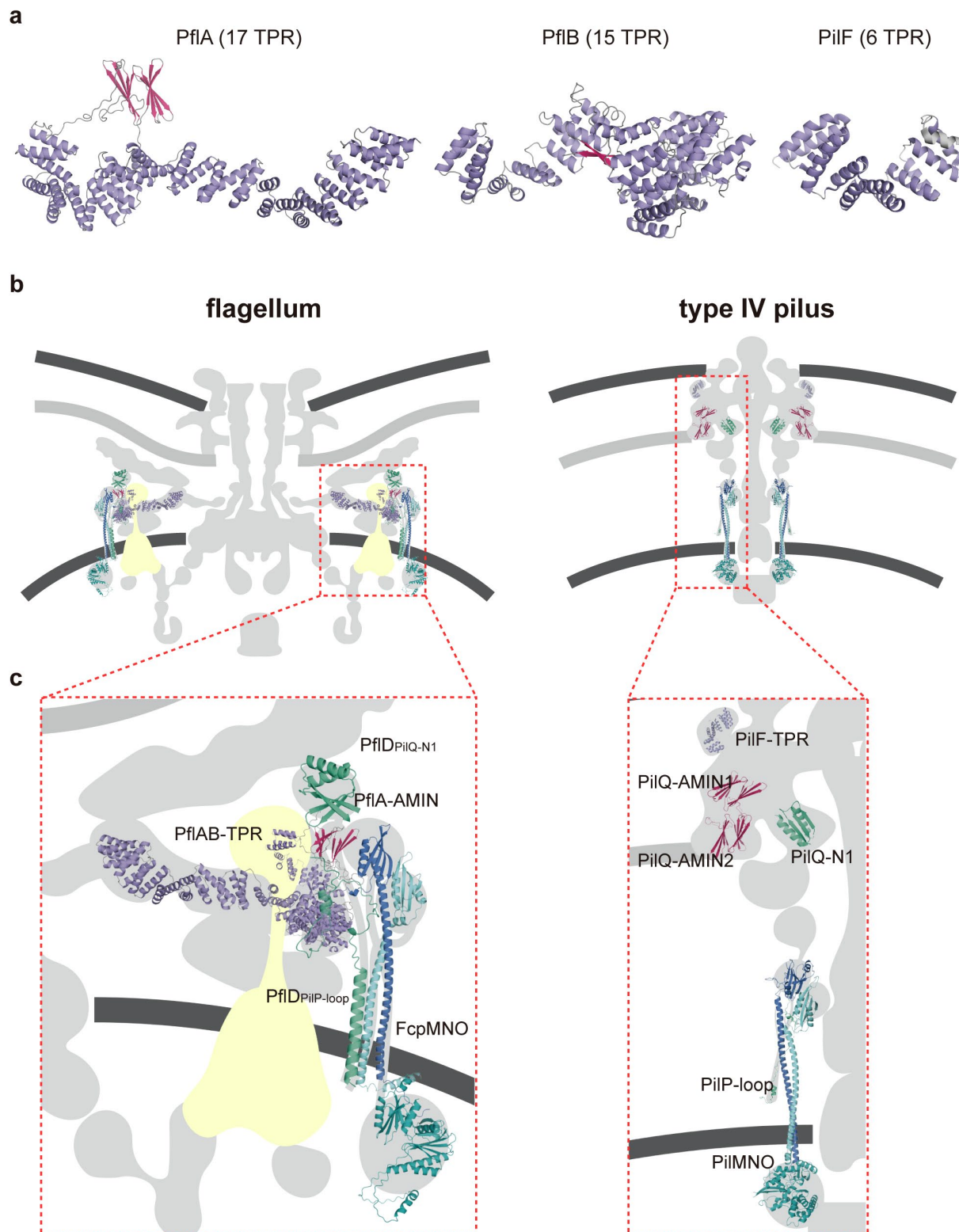
**Extended Data Figure 10. The conserved gene order of *fcpMNO* operon with its upstream genes in *Campylobacterota* genomes.** The identified gene clusters of T4P in *Campylobacterota* genomes are also shown here. Branches were highlighted for *Arcobacter* (blue) and *Nitratiruptor* (red) that have non-F3 chemosensory class and their genes of *fcpMNO* operon have fusion as indicated at the bottom of the figure.



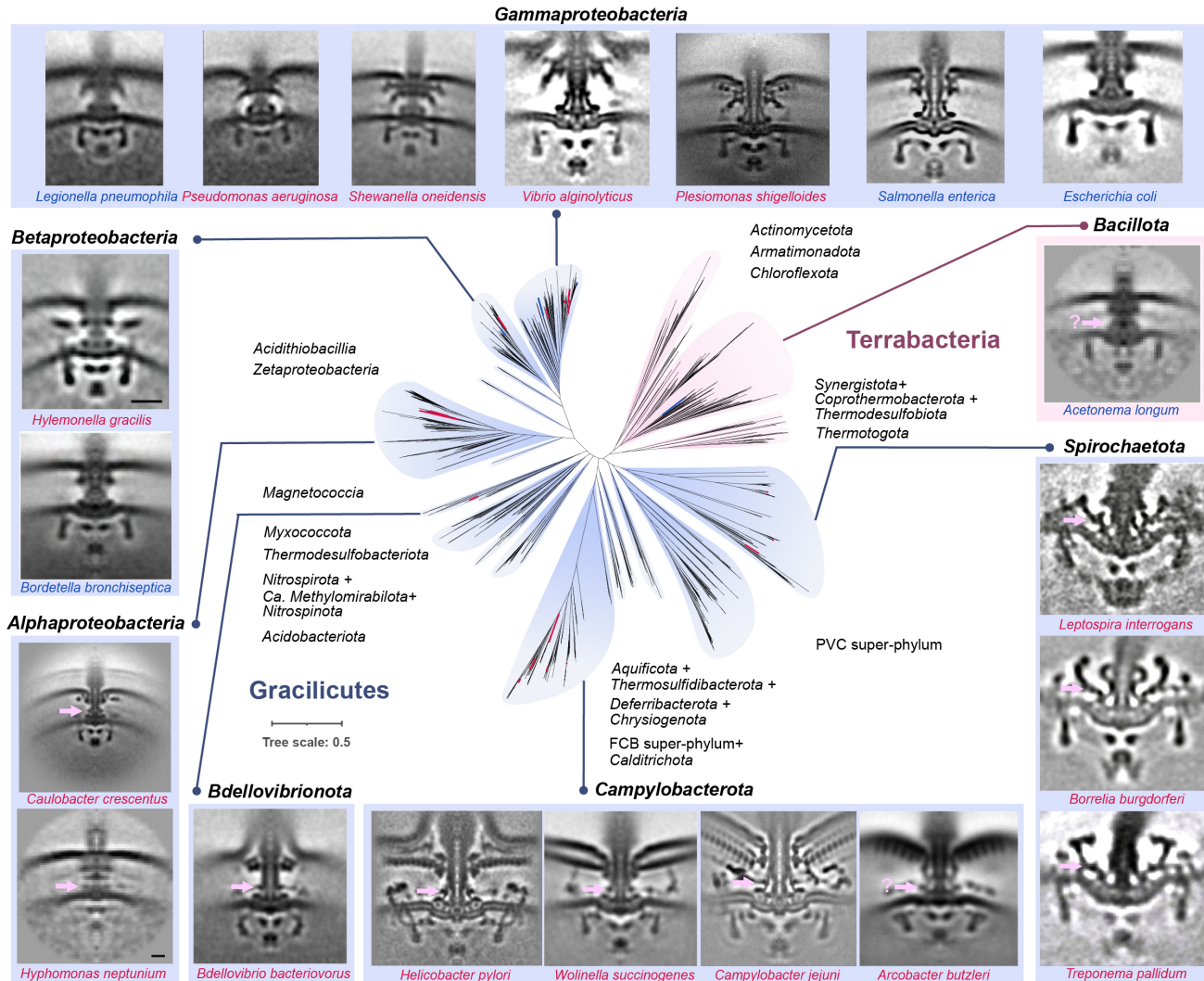
**Extended Data Figure 11. Structures of FlgY homologs and associated genomic contexts for representative species across phyla.** The transmembrane motif and signal peptide predicted by TMHMM 2.0 and SignalP 6.0 are colored in blue and green, respectively. All structures are predicted by AlphaFold3. The protein names highlighted in red on the top row are FlgY homologs that have been experimentally characterized, including MotE from both *S. meliloti*<sup>4</sup> and *C. sphaerooides*<sup>5</sup> and FlbB from *B. burgdorferi*<sup>6</sup>. CC\_2059 from *C. crescentus* is also highlighted in red since the E-ring is first identified from this species<sup>7,8</sup> and most likely CC\_2059 constitutes the E-ring.



**Extended Data Fig Figure 12. Structures of PflAB homologs and associated genomic contexts for representative species across phyla.** The transmembrane motif and signal peptide predicted by TMHMM 2.0 and SignalP 6.0 are colored in blue and green, respectively. The number of β-sheets in the β-sandwich domain is indicated above each structure. All structures are predicted by AlphaFold3. The protein names highlighted in red on the top rows are PflA or PflB homologs that have been experimentally characterized, including MotC from *S. meliloti*<sup>4</sup>, MotK from *C. sphaeroides*<sup>5</sup> and FlcAB from *B. burgdorferi*<sup>9,10</sup>. CC\_2058 from *C. crescentus* is also highlighted in red since most likely CC\_2058 interacts with CC\_2059 that constitutes the E-ring.



**Extended Data Figure 13. Structural Comparisons of homologous proteins in flagellum and T4P. a,** Structural comparison of PflA, PflB, and PilF (PDB:2FI7). **b-c,** Scaffolding components of *C. jejuni* motor share homology with T4P proteins.



**Extended Data Fig Figure 14. Summary of motor structures imaged by cryo-ET and mapped to bacterial species tree.** The phylogenetic tree in the center is derived from Fig. 6c. The motor structures investigated by cryo-ET are displayed on the periphery, with one representative species from each genus and taxon group labeled at the top of the image. Species names highlighted in blue indicate that their stator complexes are dynamic and invisible, while those marked in red represent that their stator complexes are visible. Potential E-ring is indicated by pink arrow and question marks in the image of *Acetonema longum* and *Arcobacter butzleri* mean that the position of E-ring is uncertain. Information of motor structure for species (follow a clockwise order) were taken from references: *Acetonema longum*<sup>11</sup>, *Leptospira interrogans*<sup>12</sup>, *Borrelia burgdorferi*<sup>13</sup>, *Treponema pallidum*<sup>14</sup>, *Arcobacter butzleri*<sup>15</sup>, *Campylobacter jejuni* (this study), *Wolinella succinogenes*<sup>15</sup>, *Helicobacter pylori*<sup>16</sup>, *Bdellovibrio bacteriovorus*<sup>15</sup>, *Hypomonas neptunium*<sup>11</sup>, *Caulobacter crescentus*<sup>17</sup>, *Bordetella bronchiseptica*<sup>18</sup>, *Hylemonella gracilis*<sup>11</sup>, *Legionella pneumophila*<sup>19</sup>, *Pseudomonas aeruginosa*<sup>19</sup>, *Shewanella oneidensis*<sup>19</sup>, *Vibrio alginolyticus*<sup>20</sup>, *Plesiomonas shigelloides*<sup>21</sup>, *Salmonella enterica*<sup>22</sup>, *Escherichia coli*<sup>23</sup>.

## References

- 1 Dugar, G. *et al.* High-resolution transcriptome maps reveal strain-specific regulatory features of multiple *Campylobacter jejuni* isolates. *PLoS genetics* **9**, e1003495 (2013). <https://doi.org/10.1371/journal.pgen.1003495>
- 2 Gilbreath, J. J., Cody, W. L., Merrell, D. S. & Hendrixson, D. R. Change is good: variations in common biological mechanisms in the epsilonproteobacterial genera *Campylobacter* and *Helicobacter*. *Microbiology and molecular biology reviews : MMBR* **75**, 84-132 (2011). <https://doi.org/10.1128/MMBR.00035-10>
- 3 Lertsethakarn, P., Ottemann, K. M. & Hendrixson, D. R. Motility and chemotaxis in *Campylobacter* and *Helicobacter*. *Annu Rev Microbiol* **65**, 389-410 (2011). <https://doi.org/10.1146/annurev-micro-090110-102908>
- 4 Eggenhofer, E., Haslbeck, M. & Scharf, B. MotE serves as a new chaperone specific for the periplasmic motility protein, MotC, in *Sinorhizobium meliloti*. *Molecular microbiology* **52**, 701-712 (2004). <https://doi.org/10.1111/j.1365-2958.2004.04022.x>
- 5 Velez-Gonzalez, F. *et al.* Rotation of the Fla2 flagella of *Cereibacter sphaerooides* requires the periplasmic proteins MotK and MotE that interact with the flagellar stator protein MotB2. *PloS one* **19**, e0298028 (2024). <https://doi.org/10.1371/journal.pone.0298028>
- 6 Moon, K. H. *et al.* Spirochetes flagellar collar protein FlbB has astounding effects in orientation of periplasmic flagella, bacterial shape, motility, and assembly of motors in *Borrelia burgdorferi*. *Molecular microbiology* **102**, 336-348 (2016). <https://doi.org/10.1111/mmi.13463>
- 7 Johnson, R. C., Walsh, M. P., Ely, B. & Shapiro, L. Flagellar hook and basal complex of *Caulobacter crescentus*. *Journal of bacteriology* **138**, 984-989 (1979). <https://doi.org/10.1128/jb.138.3.984-989.1979>
- 8 Stallmeyer, M. J., Hahnenberger, K. M., Sosinsky, G. E., Shapiro, L. & DeRosier, D. J. Image reconstruction of the flagellar basal body of *Caulobacter crescentus*. *Journal of molecular biology* **205**, 511-518 (1989). [https://doi.org/10.1016/0022-2836\(89\)90222-2](https://doi.org/10.1016/0022-2836(89)90222-2)
- 9 Xu, H., He, J., Liu, J. & Motaleb, M. A. BB0326 is responsible for the formation of periplasmic flagellar collar and assembly of the stator complex in *Borrelia burgdorferi*. *Molecular microbiology* **113**, 418-429 (2020). <https://doi.org/10.1111/mmi.14428>
- 10 Chang, Y., Xu, H., Motaleb, M. A. & Liu, J. Characterization of the Flagellar Collar Reveals Structural Plasticity Essential for Spirochete Motility. *mBio* **12**, e0249421 (2021). <https://doi.org/10.1128/mBio.02494-21>
- 11 Chen, S. *et al.* Structural diversity of bacterial flagellar motors. *The EMBO journal* **30**, 2972-2981 (2011). <https://doi.org/10.1038/emboj.2011.186>
- 12 Raddi, G. *et al.* Three-dimensional structures of pathogenic and saprophytic *Leptospira* species revealed by cryo-electron tomography. *Journal of bacteriology* **194**, 1299-1306 (2012). <https://doi.org/10.1128/JB.06474-11>
- 13 Liu, J. *et al.* Intact flagellar motor of *Borrelia burgdorferi* revealed by cryo-electron tomography: evidence for stator ring curvature and rotor/C-ring assembly flexion. *J Bacteriol* **191**, 5026-5036 (2009). <https://doi.org/10.1128/jb.00340-09>
- 14 Liu, J. *et al.* Cellular architecture of *Treponema pallidum*: novel flagellum, periplasmic cone, and cell envelope as revealed by cryo electron tomography. *Journal of molecular biology* **403**, 546-561 (2010). <https://doi.org/10.1016/j.jmb.2010.09.020>
- 15 Chaban, B., Coleman, I. & Beeby, M. Evolution of higher torque in *Campylobacter*-type bacterial flagellar motors. *Sci Rep* **8**, 97 (2018). <https://doi.org/10.1038/s41598-017-18115-1>

- 16 Tachiyama, S. *et al.* The flagellar motor protein FliL forms a scaffold of circumferentially positioned rings required for stator activation. *Proceedings of the National Academy of Sciences of the United States of America* **119** (2022). <https://doi.org/10.1073/pnas.2118401119>
- 17 Rossmann, F. M., Hug, I., Sangermani, M., Jenal, U. & Beeby, M. In situ structure of the Caulobacter crescentus flagellar motor and visualization of binding of a CheY-homolog. *Molecular microbiology* **114**, 443-453 (2020). <https://doi.org/10.1111/mmi.14525>
- 18 Ferreira, J. L. *et al.* The "Jack-of-all-Trades" Flagellum From Salmonella and E. coli Was Horizontally Acquired From an Ancestral  $\beta$ -Proteobacterium. *Front Microbiol* **12**, 643180 (2021). <https://doi.org/10.3389/fmicb.2021.643180>
- 19 Kaplan, M. *et al.* The presence and absence of periplasmic rings in bacterial flagellar motors correlates with stator type. *eLife* **8** (2019). <https://doi.org/10.7554/eLife.43487>
- 20 Carroll, B. L. *et al.* The flagellar motor of Vibrio alginolyticus undergoes major structural remodeling during rotational switching. *eLife* **9** (2020). <https://doi.org/10.7554/eLife.61446>
- 21 Ferreira, J. L. *et al.*  $\gamma$ -proteobacteria eject their polar flagella under nutrient depletion, retaining flagellar motor relic structures. *PLoS biology* **17**, e3000165 (2019). <https://doi.org/10.1371/journal.pbio.3000165>
- 22 Zhu, S. *et al.* In Situ Structures of Polar and Lateral Flagella Revealed by Cryo-Electron Tomography. *Journal of bacteriology* **201** (2019). <https://doi.org/10.1128/JB.00117-19>
- 23 Zhu, S. *et al.* Molecular architecture of the sheathed polar flagellum in Vibrio alginolyticus. *Proceedings of the National Academy of Sciences of the United States of America* **114**, 10966-10971 (2017). <https://doi.org/10.1073/pnas.1712489114>